Davide Donati · Doug Stead · Marc-André Brideau · Monica Ghirotti

Using pre-failure and post-failure remote sensing data to constrain the three-dimensional numerical model of a large rock slope failure

Abstract Factors governing rock slope stability include lithology, geological structures, hydrogeological conditions, and landform evolution. When certain conditions are met, rock slopes may become unstable, inducing deformation and failure. In the present study, an integrated remote sensing-numerical modeling approach investigates the deformation mechanisms leading to the 1965 Hope Slide, BC, Canada and the effect of slope kinematics on the long-term evolution of the slope. Pre- and post-failure datasets were used to perform a large-scale geomorphic and structural characterization, including kinematic and block-theory analyses. Extensive data collection was also undertaken using state-of-the-art remote sensing techniques, including digital photogrammetry (Structure-from-Motion), laser scanning (aerial and terrestrial), and infrared thermography. New evidence is provided that one or more prehistoric failures caused the removal of a key-block, and the initiation of long-term slope deformation and cumulative slope damage ultimately resulting in the catastrophic 1965 event. Detailed characterization of the rock slope has allowed the first three-dimensional, distinct element numerical model of the Hope Slide to be conducted. The results of the numerical simulations involving gradual reduction of the rupture surface shear strength indicate that 1965 slope failure may represent the outcome of a long-term, progressive failure mechanism that initiated after a prehistoric landslide. This combined field mapping–remote sensing–numerical modeling study clearly highlights the role of 3D slope kinematics on the geomorphic evolution of the slope, along with the associated failure mechanisms.

Keywords Hope Slide · Remote sensing · 3D-numerical modeling · Slope kinematics · GIS analysis

Introduction

Investigating the stability of high rock slopes is becoming increasingly important, as higher and steeper slopes are accommodating exponential population growth and increased demand for resources (Petley 2010). As part of a detailed rock slope hazard assessment, a careful geological investigation of the slope is therefore critical to identify the mechanisms that may cause the occurrence of major landslide events.

The deformation and failure of rock slopes is controlled by many interacting geological factors and processes. Geological structures, such as faults, folds, and rock mass jointing, as well as lithological features, such as bedding planes, can provide basal, rear, or lateral release to unstable volumes of rock mass (Stead and Wolter 2015). The vast majority of large landslide events were at least partially controlled by geological structures, including the Frank Slide (Humair et al. 2013), the Vajont Slide (Semenza and Ghirotti 2000; Wolter et al. 2014), and the Palliser rockslide (Sturzenegger and Stead 2012). Slope morphology can also control

the development of slope instability, by providing lateral kinematic release to potentially unstable rock slopes (Ganerød et al. 2008; Brideau 2010). The condition for which discrete blocks may be removable from the slope is generally referred to as "kinematic freedom." While geological structures with high persistence and step-path geometries formed by intersection of discontinuities are essential in providing kinematic freedom to large rock slope failures, time-dependent and dynamic processes can modify the kinematic conditions of rock slopes and enhance the mobility of landslides. For instance, the steepening of slopes due to river erosion and glacial advance and retreat can promote instability by causing stress concentration at the toe and daylighting of the basal rupture surface (Clayton et al. 2017). The progressive accumulation of damage is also critical in the evolution of slope stability (Stead and Eberhardt 2013). The action of endogenic factors, such as earthquakes (Gischig et al. 2015; Wolter et al. 2016), and exogenic factor, such as extreme weather events (Azzoni et al. 1992), and cyclic fluctuation in groundwater table (Preisig et al. 2016), causes the formation of internal and external features, referred to as slope damage, that progressively weaken the rock slope (Stead and Eberhardt 2013). Brittle fracturing of intact rock bridges may reduce kinematic constraints, causing failures to occur in otherwise stable rock slopes (e.g., Donati et al. 2019).

Due to the complex interaction of the factors described above, the identification of the mechanisms and processes underlying large-scale slope instability requires a comprehensive analysis. The introduction and improvement of remote sensing techniques has enhanced the amount and quality of geological data that can be collected. Structural and geomorphic data at various scales may be extracted from point clouds obtained from airborne and terrestrial laser scanning (ALS/TLS; Jaboyedoff and Derron 2020) or photogrammetric techniques, such as terrestrial digital photogrammetry (TDP; Birch 2006; Francioni et al. 2019) and Structure-from-Motion (SfM; Westoby et al. 2012; Vanneschi et al. 2019). Small-scale rock mass and slope damage features may also be mapped using high-resolution photography (HRP; Donati et al. 2018; Spreafico et al. 2017a). Water seepage in rock slope may be investigated using infrared thermography (IRT; Vivas 2014). Recently, IRT has been employed to identify near-surface intact rock bridges (Guerin et al. 2019). Numerical modeling is also beneficial for detailed characterization of the processes driving the deformation and failure of rock slopes. Kinematic analyses and limit equilibrium methods may be used in preliminarily investigation of the failure mechanisms and the factor of safety of a slope (Hungr and Amann 2011; Lu et al. 2016). Continuum methods, such as finite element and finite difference methods (FEM/FDM), model the material forming the slope as a continuum and are best suited to investigate problems where rock mass strength controls

slope failure (Grøneng et al. 2010; Riva et al. 2018). In recent years, continuum-based numerical modeling codes have been introduced that are capable of implementing discontinuities within a finite element or a finite difference mesh, making them capable of simulating fractured rock masses (Hammah et al. 2007; Spreafico et al. 2017b). Discontinuum methods, such as the distinct element method (DEM), consider the material as an assembly of blocks that can rotate, slide, and detach from each other, and have been largely employed for the analysis of slopes where the stability is governed by structures and block interaction (Havaej et al. 2016). Hybrid finite-discrete element methods (FDEM; Munjiza et al. 1995) and lattice-spring methods (Cundall 2011) have been introduced to investigate the role of the brittle fracturing of rock on the stability of a slope. Increasingly sophisticated numerical modeling methods allow more complex failure mechanisms to be modeled; in turn, their use requires input data that are both more sophisticated and challenging to collect (Stead and Coggan 2012).

In the present paper, an integrated remote sensing-numerical modeling approach was used for the investigation of a major rock slope failure, the 1965 Hope Slide, in British Columbia, Canada. First, several remote sensing techniques and approaches were employed to investigate the structural and geomorphic setting of the slope and analyze its kinematic configuration. A re-interpretation of the slope failure is provided highlighting the role of a large, pre-historic event that occurred at the same site on the long-term stability evolution of the slope and the progressive accumulation of slope damage. A three-dimensional, distinct element numerical analysis is performed to investigate the role of the geological structures and progressive cohesion degradation on the long-term stability and deformation of the rock slope. Using such an integrated approach, we highlight the role of slope kinematics on the stability of high rock slopes, and the importance of using three-dimensional numerical methods in the investigation of structurally controlled slope failures.

The Hope Slide

History of the slide

The Hope Slide involved a volume of 48 million m³ of rock and it is the second largest historical rock avalanche in Canada. The slope failure occurred, in two stages, early in the morning of January 9, 1965, between 4:00 AM and 7:15 AM (Anderson 1965). The slide affected the southern slope of the Johnson Ridge, 15 km east of the municipality of Hope, in British Columbia, between a ground elevation of 870 and 1800 m above sea level (a.s.l.), (Mathews and McTaggart 1969) (Fig. 1a). The slide debris completely filled the Outram Lake, located at the base of the slope, climbed up the opposite side of the Nicolum Valley, and traveled down valley for about 2 km. The rock slope failure intersected and buried the Hope–Princeton Highway, raising the valley floor up to 60 m above its original elevation, and killing four people (Anderson 1965). Two low-intensity earthquakes (M = 3.2 and M = 3.1) were registered at the Penticton seismic station (120 km east of the Hope Slide) at the same time as the failures and were initially proposed as the trigger mechanism for the failure (Mathews and McTaggart 1969). The hypothesis was initially confuted by Wetmiller and Evans (1989), who observed that larger earthquakes registered in the area failed to trigger major slope failures. A seismic

trigger was later shown to be incorrect by Weichert et al. (1994), who also suggested that the two earthquakes were the result, rather than the cause, of the slope collapse. The 1965 event occurred on the same slope as a pre-historical failure (Cairnes 1924) of similar volume (Mathews and McTaggart 1969). Evans and Couture (2002) excavated trenches to investigate the stratigraphy of the material above the 1965 headscarp and concluded that the event was not an episodic failure, but rather the catastrophic outcome of a progressive, long-term deformation of the slope.

Presently, the activity of the slope is predominantly characterized by small rockfalls occurring at the intersection of fault-damage zones and the headscarps. Several events were observed while the photogrammetric surveys described in the present study were being undertaken, particularly along the lateral scarp. InSAR investigations have also shown that marked displacement is occurring at the upper headscarp, although within limited, localized areas (Hosseini et al. 2018). Similar deformation was also recognized by von Sacken (1991), who observed the opening of a tension crack behind the headscarp. Slow deformation was also observed within the debris field and has been interpreted possibly as a result of the consolidation of sediments at depth due to surcharge by the 1965 deposit, or a slow-moving creep that developed within the Hope Slide debris (Hosseini et al. 2018).

Geological and structural overview

The Hope Slide is located within the Northern Cascades Mountain Range, in southern British Columbia. The slide area is presently bounded on the northern and northwestern sides by sub-vertical slopes, up to 150 m high, which define the lateral scarp and upper headscarp, respectively. The rupture surface dips in a westward direction at an angle of 30°. The basal sliding surface is largely covered by debris, except for a steeper, 200 m by 150 m area in the central part of the slope, where the bedrock outcrops (Fig. 1b).

The slope is formed by Paleozoic greenstone of the Hozameen Complex, a weakly metamorphosed mafic volcanic rock (Fig. 1c, d). The rock is massive in nature, and the volcanic texture and structure have been obliterated by metamorphic recrystallization (McTaggart and Thompson 1967). Locally, the greenstone is intruded by sills and dikes of felsite, an aphanitic, volcanic rock that occurs as pinkish and buff color varieties. Buff felsite is organized in sills dipping out of the slope. Two such sills clearly stand out within the daylighting portion of the rupture surface (Fig. 1d). Felsite–greenstone lithological contacts appear to be sharp and devoid of gouge, except within or close to tectonic structures (faults and shear zones), where clay-rich infill can be observed (Brideau et al. 2005).

The slide area is traversed by several NNW–SSE striking faults that form gullies and crevices on both sides of the Johnson Ridge (Fig. 1a). Von Sacken (1991) suggested that the structures controlled the behavior of the slide, and that one of the faults divided the volumes that failed in the two stages of the 1965 event. Brideau et al. (2005) further investigated the structurally controlled nature of the slope failure, suggesting that tectonic shear zones may have acted as lateral release surfaces along the northern and southern boundaries of the slide. They also observed changes in orientation of the basal rupture surface, which were associated with a regional scale synform.
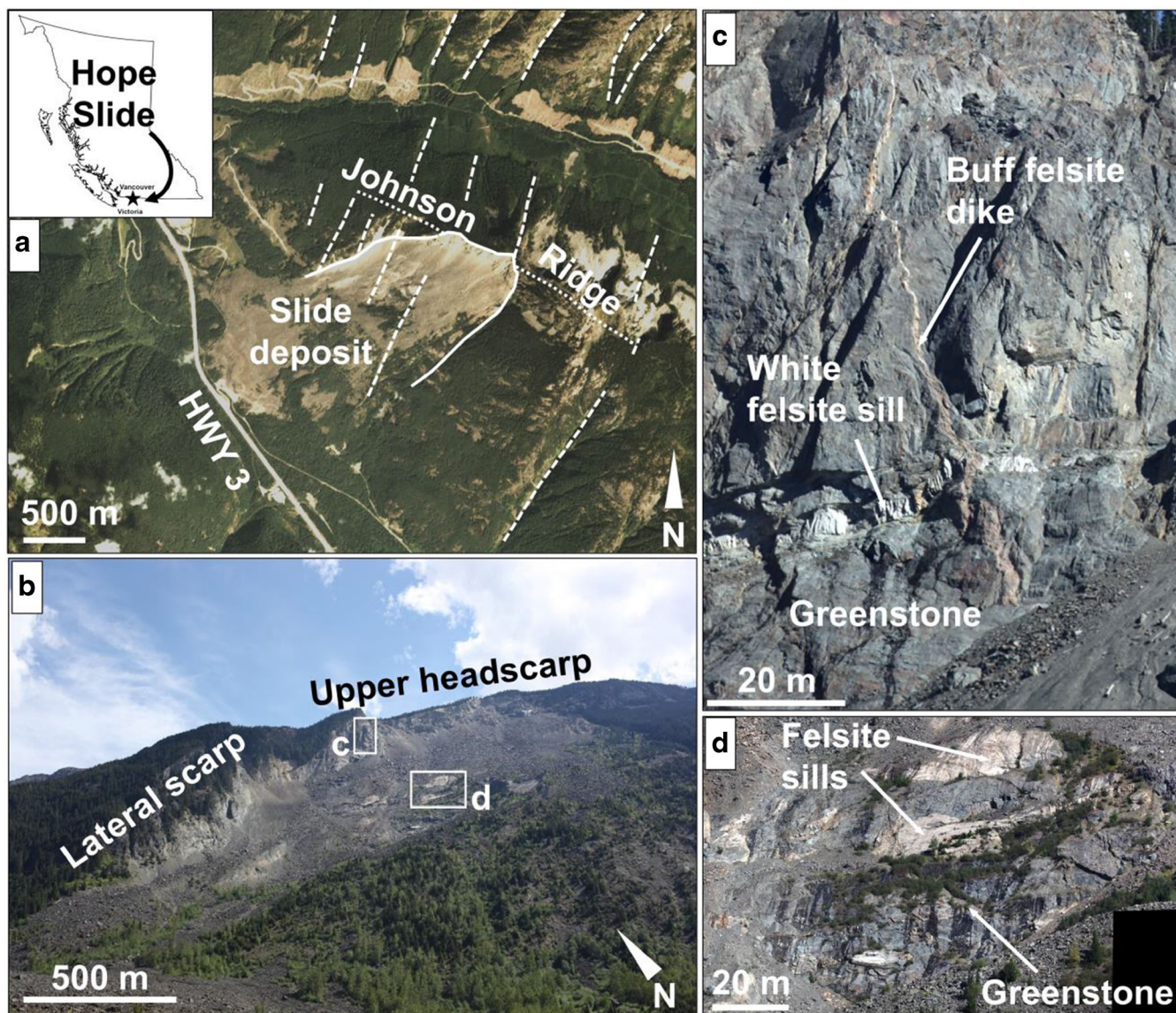
Fig. 1 Geographic and lithological overview of the Hope Slide. a 2018 satellite image (Planet Team 2019) of the slide area. Dashed lines indicate linear structural features. Dotted curve outlines the Johnson Ridge. Solid line shows the boundary of the 1965 slide area. In the inset, the star indicates the location of the Hope Slide in British Columbia. b View of the slide area from the viewpoint at the base of the slope (photograph summer 2015). c, d Detail of the rock mass and lithology contacts along the lateral scarp and within the daylighting part of the rupture surface (photographs taken fall 2011)

Methods

The investigation of the rock slope involved in the 1965 event was undertaken at progressively larger scales, in order to characterize the slope in an increasingly higher level of detail. The workflow proposed in Donati et al. (2017) was followed for the data collection and processing, and is summarized in Fig. 2.

Slope-scale structural and geomorphic characterization

We reviewed and processed both existing and new data to assess the long-term evolution of the slope, and the potential underlying mechanisms. A set of historical aerial photographs taken in 1961 (4 years prior to the event) was obtained from the Province of British Columbia database (roll BC4014, frames 21–25), and a pre-failure

DTM with 10 m resolution was reconstructed using a SfM approach in Photoscan (Agisoft LLC 2018; Fig. 3). Easily identifiable natural points outside of the area affected by the slide were selected in the pre-failure imagery, and their location obtained from the 2015 ALS dataset that was made available for the present study by the Ministry of Transportation and Infrastructure (MoTI) of British Columbia.

The pre- and post-failure topographic surfaces were employed to characterize structural and geomorphic features within the area of interest, and to investigate the relationship between first-order geological structures and slope stability. The analysis was undertaken in ArcGIS 10.5 (ESRI 2017), where hillshade, aspect, and slope maps of the pre- and post-failure DTMs were created and used to perform lineament mapping (e.g., Donati et al. 2020;
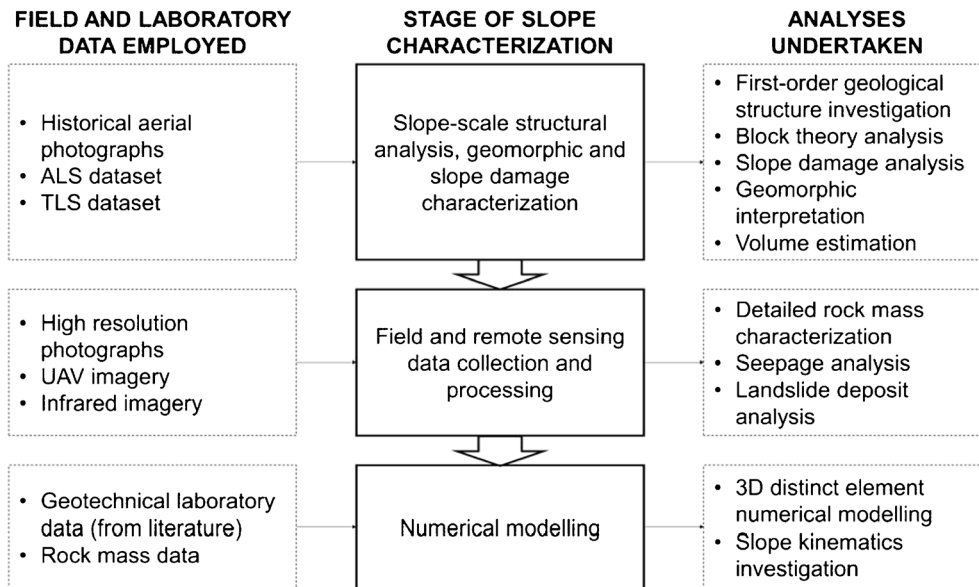
FIELD AND LABORATORY DATA EMPLOYED	STAGE OF SLOPE CHARACTERIZATION	ANALYSES UNDERTAKEN
• Historical aerial photographs • ALS dataset • TLS dataset	Slope-scale structural analysis, geomorphic and slope damage characterization	• First-order geological structure investigation • Block theory analysis • Slope damage analysis • Geomorphic interpretation • Volume estimation
• High resolution photographs • UAV imagery • Infrared imagery	Field and remote sensing data collection and processing	• Detailed rock mass characterization • Seepage analysis • Landslide deposit analysis
• Geotechnical laboratory data (from literature) • Rock mass data	Numerical modelling	• 3D distinct element numerical modelling • Slope kinematics investigation

Fig. 2 Workflow of the investigation conducted at the Hope Slide. The slope characterization has been performed by progressively increasing the level of detail

Francioni et al. 2018). The long-term evolution of the slope considering the prehistoric event that affected the slope (Mathews and McTaggart 1969) was investigated, from a kinematic perspective, by performing a block-theory analysis (Goodman and Shi 1985).

A volume estimation was also undertaken, by comparing the elevation change between the pre- and post-failure models. For this analysis, both the TLS and the ALS dataset were employed, and the resulting volume computations compared. The TLS
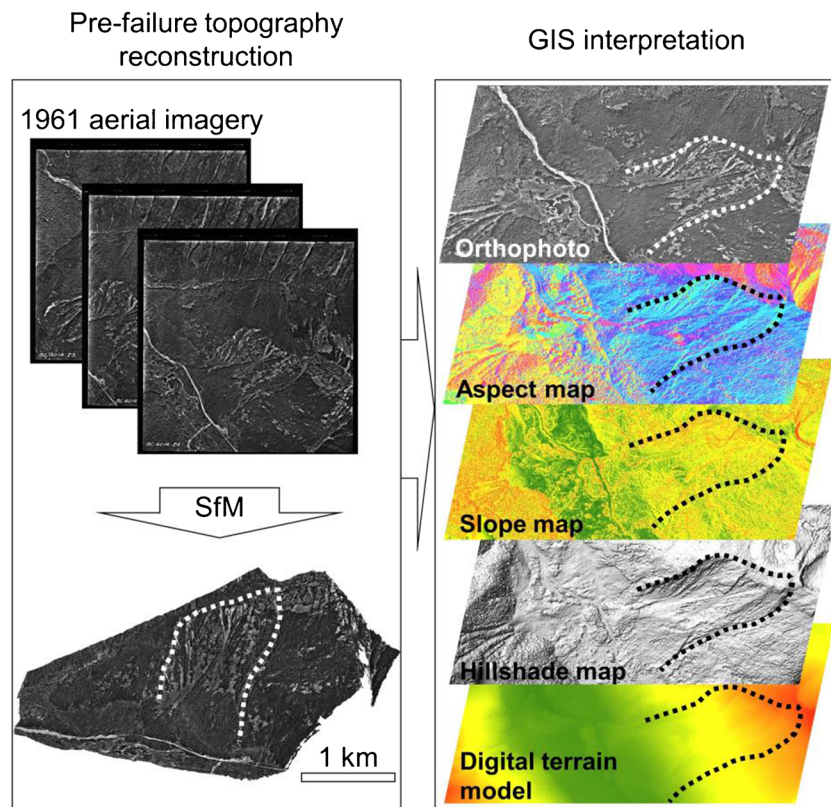

Fig. 3 Conceptual workflow for the reconstruction and analysis of the pre-failure slope topography. The 1961 historical aerial imagery was processed using a SfM approach to obtain the pre-1965 slope geometry. The dotted curve outlines the area affected by the slide

dataset was collected using a Riegl VZ-4000, full-wave form TLS characterized by a maximum operating range of 4000 m (Fig. 4a). The raw dataset was first pre-processed in RiSCAN Pro 2.6 (Riegl LMS GmbH 2018), then CloudCompare 2.10 (2019) was used to build a high-resolution DTM of the slide area and the headscarp.

Outcrop-scale remote sensing characterization

A detailed characterization of the slide area was performed using both remote sensing and traditional field methods. The use of remote sensing techniques allowed for large amounts of high-resolution data to be collected from a distance. Traditional field work procedures were employed to collect discontinuity surface data, such as roughness, infilling, and alteration conditions. In the present study, the outcrop-scale characterization of the slope was conducted using primarily TLS, photogrammetric techniques, and IRT.

The detailed geomechanical characterization of the rock mass was performed using the TDP technique. Photographs of the lateral scarp and headscarp were collected using a Canon EOS 5D Mark II, 21 Mega Pixel digital single-lens reflex (DSLR) camera with an f = 400 mm focal length lens (Fig. 4b). 3D models were constructed and discontinuities mapped using 3DM Analyst mapping suite 2.5 (AdamTechnology 2017). Discontinuity spacing, persistence, and orientation were obtained from the models, and the results were compared with the trend of lineaments mapped during the large-scale investigation.

A preliminary analysis of the groundwater seepage was performed using the IRT technique, which allows for the infrared (IR) radiation emitted by an object to be captured and converted into a temperature value. In the present study, a FLIR SC7750 was employed (Fig. 4c), and thermal imagery was processed using Research IR (FLIR Systems Inc. 2015).

A block size distribution analysis of the slide deposit was undertaken using a UAV-SfM (unmanned aerial vehicle-SfM) approach. A DJI Phantom 3 Pro Quadcopter (Fig. 4d) was employed to collect imagery along a pre-determined flight path, designed to provide an 80% overlap between adjacent images. A total of 680 photographs were collected, covering an area of 2 km² of debris deposit at the base of the slope. The photographs were then processed using Photoscan software, and the obtained orthorectified image was used to perform the block size analysis.

The surface area covered by each remote sensing datasets collected and/or processed during the present study, as well as the survey stations, are outlined in Fig. 5. For each dataset, Table 1 summarizes the resolution and the intended application.

Numerical modeling

The main objective of the simulations was to investigate the role of slope kinematics on the behavior and long-term evolution of the Hope Slide. The data obtained from field mapping and analysis of both historical imagery and remote sensing surveys were used as input in the numerical modeling of the 1965 Hope Slide. Material and discontinuity properties assigned in the model were obtained from geotechnical laboratory test results, including direct shear tests performed on fault gouge, performed and described in previous studies (Brideau et al. 2005; von Sacken 1991). However, the residual friction angle for the lower order discontinuities (i.e., rock mass jointing) were defined through a trial-and-error approach,

based on the overall behavior of the model, and its ability to realistically reproduce the failure.

Results

Slope-scale characterization

Structural investigation
The analysis of the ALS dataset using hillshade, slope, and aspect maps allowed for the identification and mapping of slope-scale structural lineaments (Fig. 6a). Over 200 lineaments were mapped and their bearing computed in ArcGIS. The orientations were plotted in a rosette diagram, which show that three orientation trends occur across the slide area, referred to as I (025°), II (070°), and III (125°) (Fig. 6b). The NNE-trending faults that intersect the lateral scarp can be ascribed to trend I. The lateral scarp itself appears to be formed by the intersection of trend I and trend II lineaments. Conversely, the orientation of trend III is roughly parallel to the upper headscarp, suggesting that this feature is structurally controlled by ESE- to SE-trending geological structures. In the upper slope, the headscarp intersects three counterscarps roughly oriented parallel to lineament trend III, suggesting that these are at least partially structurally controlled (Fig. 6c).

Presently, the slide area is largely covered in debris, precluding identification of structural lineaments except for the outcropping part of the rupture surface in the central part of the slope. Therefore, the pre-failure DTM created based on the historical aerial photographs was used to investigate the structural configuration of the part of rock slope that failed in 1965. From the analysis of the hillshade, aspect, and slope maps, six large, first-order structural features were identified within the slide area and denoted as L1 to L6. The first-order structures subdivide the slide volume into five slide blocks, progressively numbered from the bottom of the slope to the crest, B1 to B5 (Fig. 7a–c).

A large-scale block theory investigation was then performed using the identified first-order structures. Block theory analysis identifies all the blocks that may potentially form within a simplified slope and classifies them into "stable," "unstable," "infinite," and "key" blocks (Goodman and Shi 1985). The objective of the analysis was to identify key blocks, the removal of which may have caused the remaining blocks to fail retrogressively. According to von Sacken (1991) and Brideau et al. (2005), the basal release surface of the Hope Slide was formed by a discontinuity set subparallel to the slope, which was therefore included in the block theory investigation. The analysis shows that block B1 represents a key block for the slope, and its removal would allow the subsequent failure of blocks B2 to B5 (Fig. 7d).

Geomorphology of the slope before the failure
The 1961 aerial photographs show abundant evidence of slope activity prior to the 1965 Hope Slide. At the base of the slope, a large, vegetated debris fan can be observed, which exceeds the elevation of the surrounding valley floor by about 60 m (profiles B–B′ and C–C′ in Fig. 8a, c). It is currently unclear whether its formation was caused by a single, relatively large event or rather a prolonged accumulation of material caused by debris flows and rockfalls under varying climatic conditions. The former Outram Lake, which was subsequently completely filled by the 1965 Hope
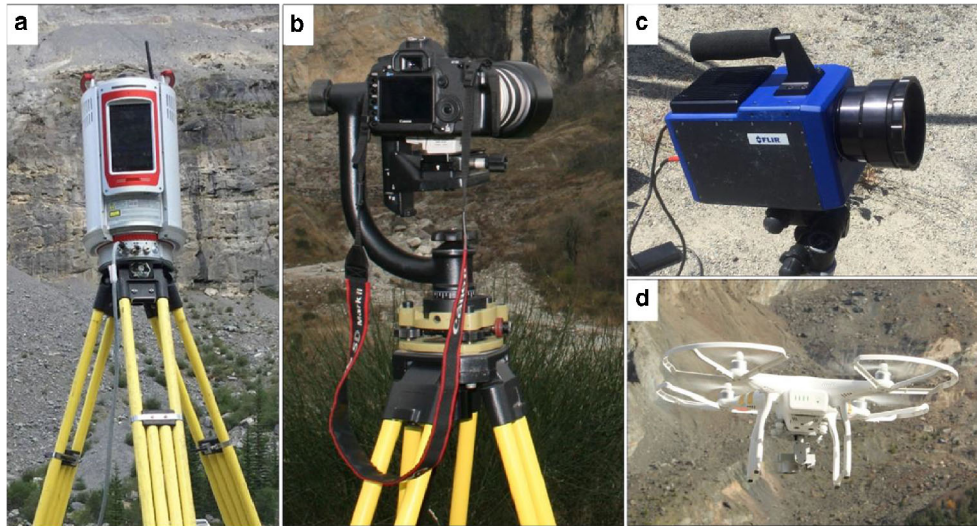
Fig. 4 Remote sensing equipment employed for the investigation of the Hope Slide. a Riegl VZ-4000 terrestrial laser scanner; b Canon EOS 5D Mark II DSLR camera with f = 400 mm focal length lens, mounted on a panorama frame; c FLIR SC7750 thermal camera with f = 100 mm focal length lens; d DJI Phantom 3 Pro Quadcopter

Slide, is located in front of the fan and lies on the deposit of a prehistoric landslide (Cairnes 1924; Mathews and McTaggart 1969). The elevation of the lake was about 710 m a.s.l. in 1961, and at its downstream side the valley floor was located at a ground elevation of 750 m a.s.l. In this elevated area, a hummocky morphology can be observed in the aerial photograph, and boulders appear to be scattered throughout the area (Fig. 8b). About 550 m northwest from the lake, the valley floor elevation drops to about 680 m a.s.l., possibly outlining the edge of the ancient landslide deposit (profile A–A′ in Fig. 8a, c). Radiocarbon analyses on organic material

Fig. 5 Location of the remote sensing stations (photograph from Google Earth). Dots identify the camera stations used for the TDP survey of the headscarp; the star marks the location of TLS and IRT stations; polygons outline the areal coverage of each survey, including the surface of the slide deposit investigated using UAV-SfM. Historical imagery SfM datasets extend beyond the boundaries of the photograph

collected below the deposit yielded an age of 9680 years B.P., which marks a minimum age for the event (Mathews and McTaggart 1978).

Several rockfall source areas can be identified between elevation 1130 m a.s.l. (near the northern boundary of the 1965 slide area) and 1740 m a.s.l. (below the upper 1965 headscarp). Mathews and McTaggart (1969) suggested that the cliffs bounding the pre-1965 active slide area also outline the headscarp of the prehistoric landslide event. From the source areas, active debris channels follow the steepest path toward two main deposition areas. The first deposition area is located above the debris fan at the base of the slope and accommodates rockfall material from the northeastern sector of the active area. The second deposition area is located on a structural ledge in the central part of the slope. This accumulation area is clearly visible in the pre-1965 slope map, in the form of a flat surface 300 m wide and up to 150 m long. Cliffs, debris channels, and accumulation areas are largely free of vegetation, in view of their active state as captured in the 1961 aerial photographs, whereas a dense canopy existed elsewhere within the slope (Fig. 8d).

The analysis of the pre-1965 aspect map shows a series of counterscarps in the upper portion of the slope, partially or completely free of vegetation (Fig. 8d). These features were truncated during the failure, as noted in the ALS dataset (Fig. 6c). Such external slope damage features have been associated with the evolution of deep-seated gravitational slope deformations of sackung type (Agliardi et al. 2012; Ambrosi and Crosta 2006). The uppermost counterscarp was only partially involved in the 1965 event and presently shows evidence of slope movements (von Sacken 1991). In addition, geomorphological field analyses showed evidence of a long-term deformation that was ongoing prior to the 1965 slope failure, suggesting that the 1965 event represents the catastrophic outcome of a sagging rock slope (Evans and Couture 2002).

A visual analysis of the 1961 aerial photographs shows the presence of a prominent cliff, located at the boundary between
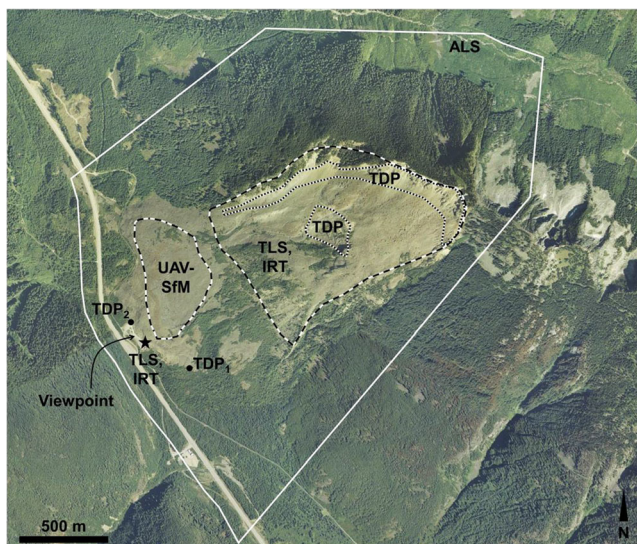
Table 1 Summary of coverage, detail, and use of the collected datasets

| Remote sensing technique	Coverage	Resolution of the dataset	Purpose of the analysis
ALS	Entire slide area and surroundings	Cell size: 1 m	Large-scale structural analysis (post-event lineament mapping) Volume estimation (post-failure slope surface)
SfM (historic aerial photograph imagery)	Entire slide area and surroundings	Point spacing: 5–10 m	Large-scale structural analysis (pre-event lineament mapping) Pre-event geomorphic analysis Volume estimation (pre-failure slope surface)
TLS	Entire sliding surface, including lateral scarp and upper headscarp	Point spacing: 20–40 cm	Volume estimation (post-failure slope surface)
TDP	Lateral scarp and upper headscarp, daylighting part of the sliding surface	Ground pixel size: 3 cm Point spacing: 10–20 cm	Discontinuity mapping and detailed rock mass characterization
UAV-SfM	Landslide deposit	Point spacing: 10 cm	Deposit block size analysis
IRT	Entire sliding surface, including lateral scarp and upper headscarp	Ground pixel size: 20–30 cm	Seepage investigation
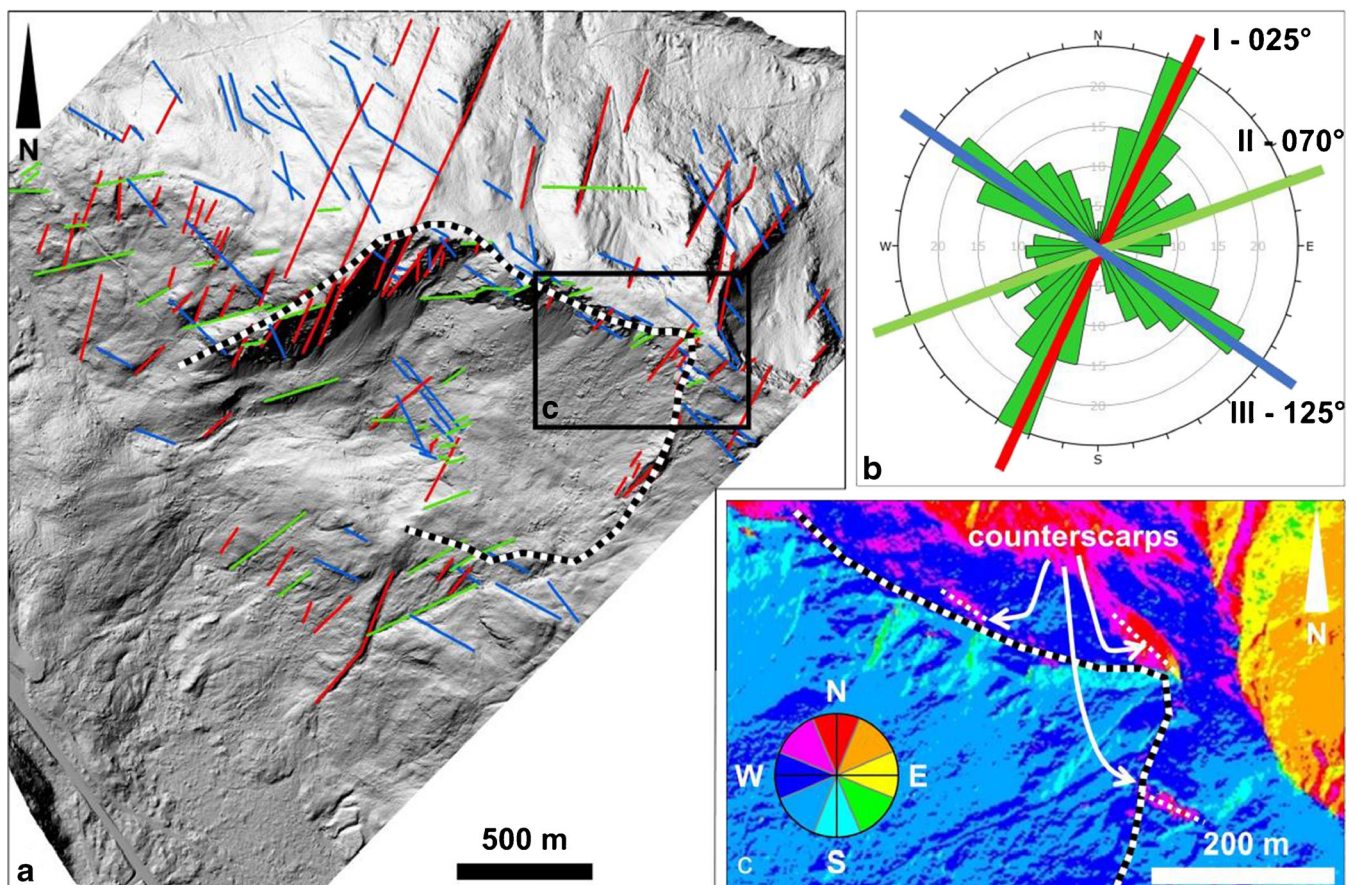
Fig. 6 Summary of the lineament analysis conducted on the ALS post-failure DTM of the Hope Slide. a Map of lineaments, color-coded based on the trend orientation. The dotted outline represents the boundary of the failed slope. The square window outlines the area represented in (c). The basemap is the hillshade view of the ALS dataset. b Rosette diagram of the lineaments. The principal lineament trends are highlighted and colored based on the trends observed in (a). c Aspect map of the western headscarp, showing the intersection with counterscarps with trend similar to III
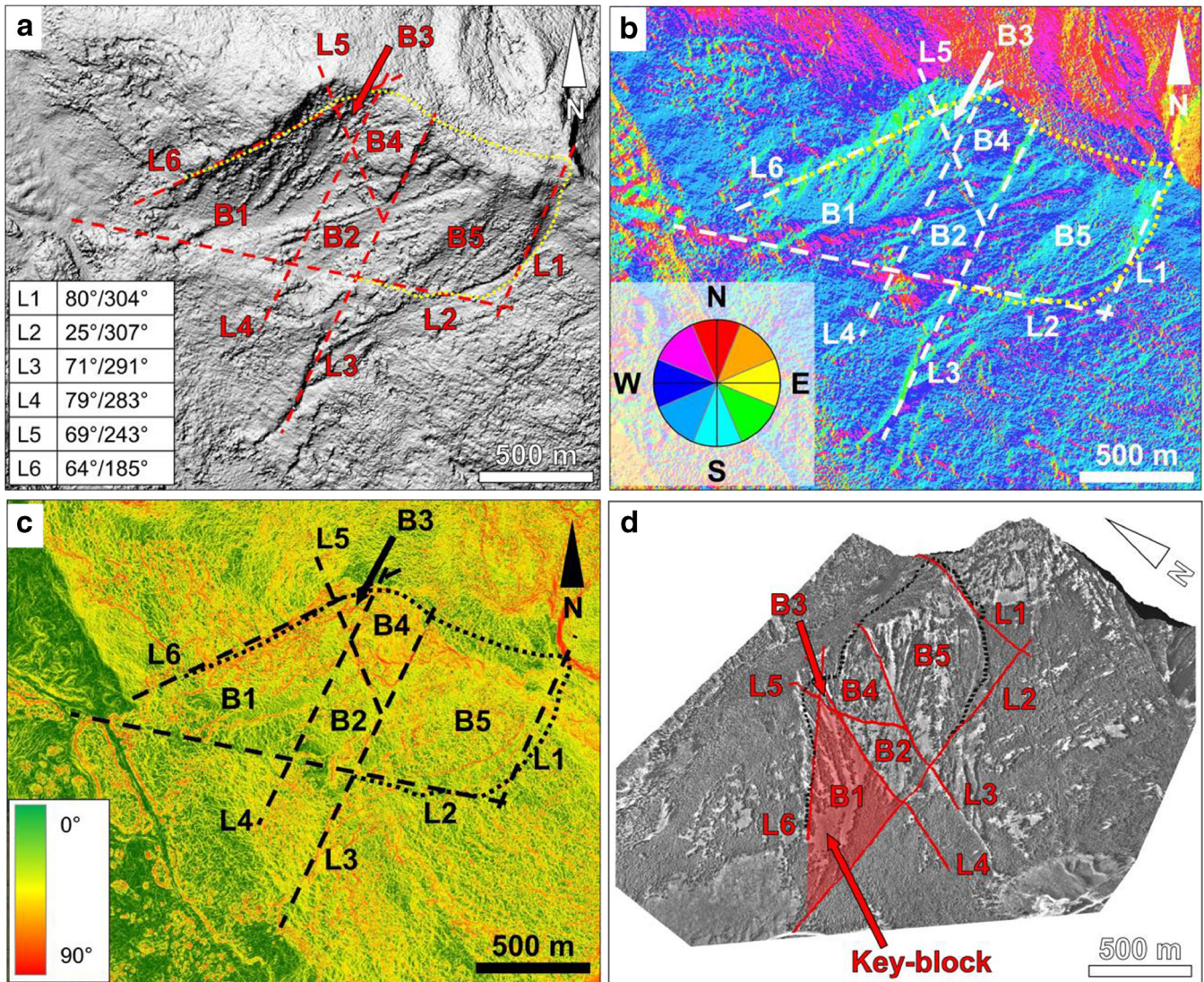
Fig. 7 Summary of the lineament analysis conducted on the SfM pre-failure DTM of the Hope Slide. a hillshade map. The inset table displays the orientation (dip/dip direction) of the mapped geological structures; b aspect map; c slope map; d imagery draped onto pre-failure 3D model. Note that B1 has been interpreted as a key block. In each map, dashed lines represent the mapped first-order lineaments, and the dotted curve outlines the area involved in the 1965 event. Lineaments are labeled from L1 to L6, blocks from B1 to B5

slide blocks B2 and B5, which is recognizable in the slope both in the pre- and post-failure imagery (Fig. 9a). This evidence suggests that only a minor volume of material originated from the section of the slope below this cliff feature. We propose that the prehistoric slope failure involved the detachment of slide blocks B1 and B2, with only limited contribution of material from the upper blocks, and, conversely, the 1965 event predominantly involved the failure of blocks B4 and B5 (Fig. 9b).

Volume estimation

The volume and the thickness of the material involved in the 1965 Hope Slide event was estimated by subtracting the pre-failure DTM (obtained from the SfM model) from the post-failure topography within the slide area (Fig. 10a–d). For the volume calculation, the ALS and TLS datasets were considered independently.

First, all datasets were registered considering the ALS as the reference surface. The volume was calculated using a cut-fill analysis in ArcGIS 10.5. A total volume loss of 47.8×10^6 m^3 and 46.5×10^6 m^3 was computed using the ALS and TLS ground surface, respectively. The differences are probably related to the presence of occlusions within the TLS dataset, which resulted in local surface interpolation during the creation of the DTM. In both cases, the maximum thickness of the slide was observed in the upper portion of the slope, within block B5 (141 m) and block B4 (134 m). Within blocks B1, B2, and B3, the maximum elevation difference ranges between 24 and 53 m (Fig. 10c). The volume of the blocks forming the slide were separately investigated, and it was noted that the upper blocks (B4 and B5) comprised approximately 80% of the volume lost during the 1965 failure. The contribution to the estimated volume loss from the lower slope in the
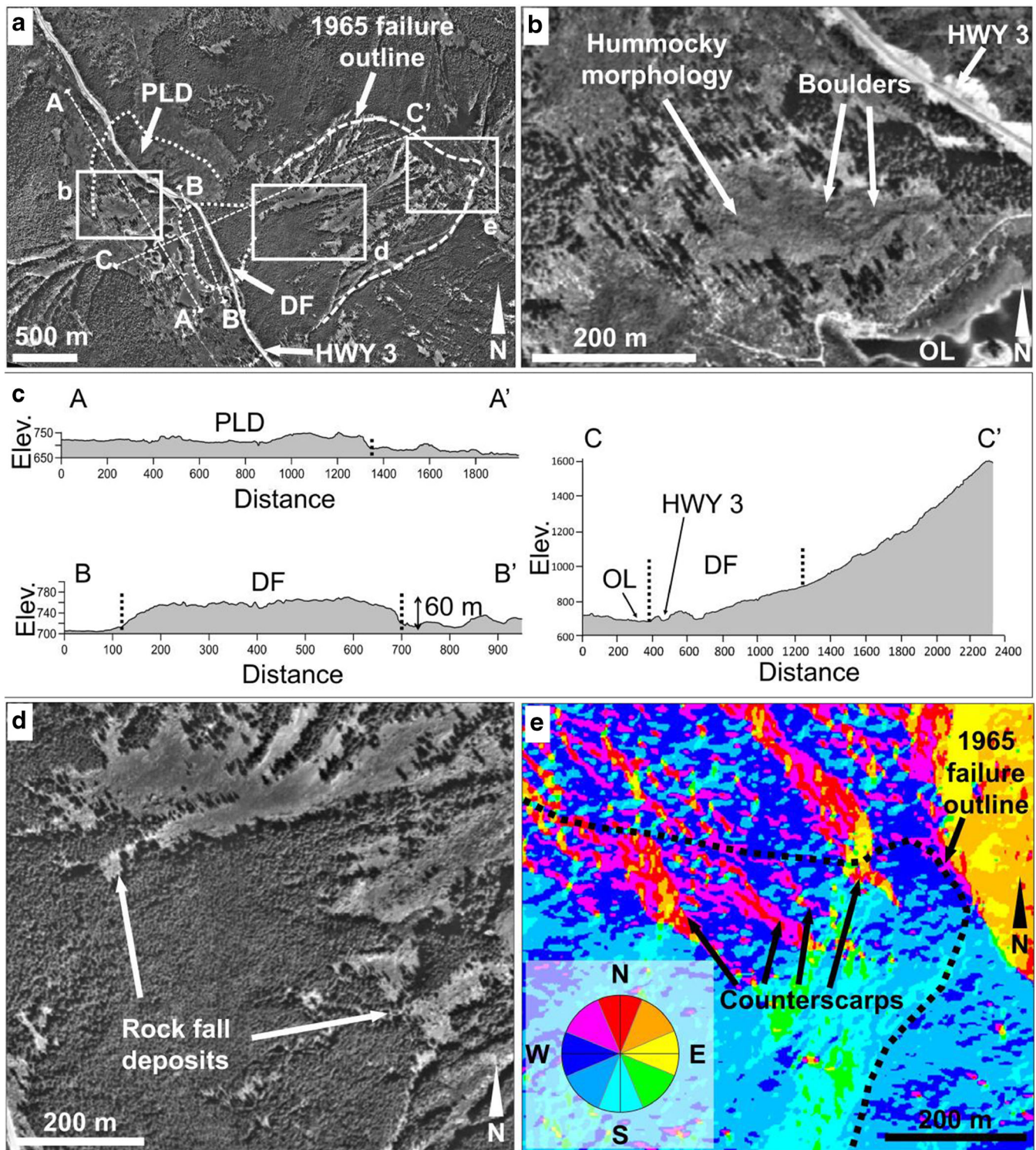
Fig. 8 Pre-failure geomorphic and slope damage analysis of the Hope Slide slope (photographs 1961). a Orthorectified image obtained from the SfM model, showing the location of the investigated profiles and outlining prehistoric landslide deposit (PLD) and debris fan (DF). The former highway 3 (HWY 3) is also labeled. b Detail of the orthorectified image showing the surface of the prehistoric landslide deposit. The hummocky morphology north of the former Outram Lake (OL) and the boulders scattered throughout the deposit are labeled. c Interpreted profiles traced in the orthorectified image, highlighting the inferred northern edge of the prehistoric landslide deposit (A–A') and the morphology of the debris fan at the base of the slope (B–B', C–C'). d Detail of the rockfall deposition areas recognized in the pre-failure slope, located above the debris fan in the lower slope, and on a structural ledge located mid-slope. e Aspect map of the upper pre-failure slope from the SfM model, highlighting the counterscarps resulting from slow, long-term slope deformation
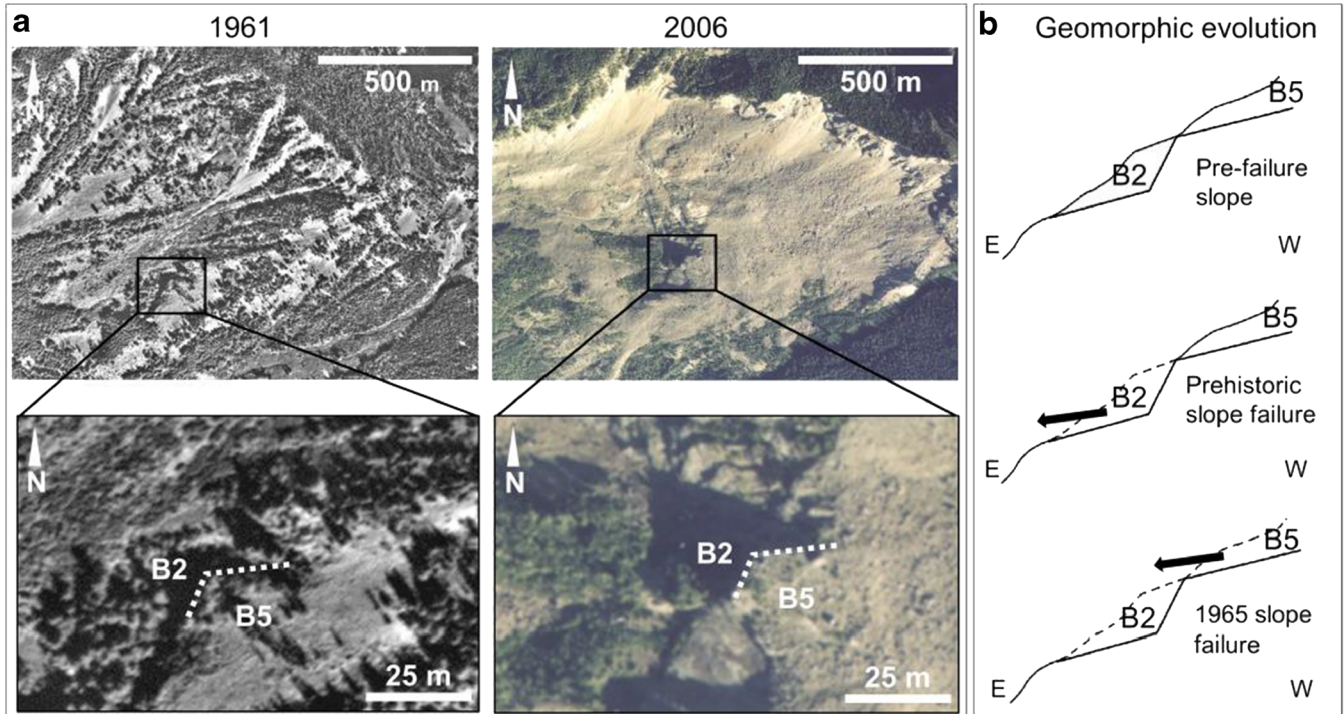
Fig. 9 Pre- and post-failure aerial photograph comparison. a Location of the geomorphic feature observed in both pre- and post-failure imagery, identified at the boundary between blocks B2 and B5. b Conceptual reconstruction of the formation of the feature highlighted in (a)

1965 event (20% of the total volume) may be constituted by loose material incorporated during the failure.

The volume loss computed in this research agrees well with previous estimations, which ranged between 47.3×10^6 m³ (Mathews and McTaggart 1969) and 48.3×10^6 m³ (von Sacken 1991). These calculations were based on the same isopach map described in Mathews and McTaggart (1969), created by computing the difference between topographic maps prior to and after the 1965 event.

Outcrop-scale rock mass and debris characterization

Rock mass characterization
The objective of the detailed remote sensing investigation was to collect rock mass discontinuity data including orientation, persistence, and spacing. The characterization was undertaken using TDP, performed on the lateral scarp and upper headscarp, and the daylighting portion of sliding surface at mid-slope. Over 1600 discontinuities were mapped in the 3DM Analyst software, and their orientation plotted on stereonets using DIPS (Rocscience 2016). Three main discontinuity sets were identified, namely, J1, J2, and J3. J1 is sub-parallel to the slope surface (30°/245° dip/dip direction on average) and likely provided a basal rupture surface for the 1965 event (Brideau et al. 2005; von Sacken 1991), and possibly also for the prehistoric failure. Discontinuity sets J2 and J3 (76°/297° and 84°/350° on average, respectively) are both sub-perpendicular to J1 (Fig. 11a). Virtual scanlines were also traced on photogrammetric models at various locations along the lateral

scarp and the upper headscarp, to characterize the discontinuity persistence and spacing. The average persistence of the identified discontinuity sets is 16 m, 10 m, and 11 m for J1, J2, and J3, respectively. Both discontinuity sets J1 and J2 are closely spaced within the slide area, whereas spacing for the set J3 is uncertain due to limited discontinuity visibility and unfavorable orientation for estimation. The structural analysis suggested that five structural domains are present within the slide area, which are approximately delineated by the first-order geological structures identified in the slope-scale structural and geomorphic analysis. Throughout the domains, a progressive counter-clockwise rotation of the main discontinuity sets can be recognized between the headscarp and the base of the slope (Donati et al. 2013). Von Sacken (1991) also observed a change in the orientation of the discontinuities between the upper and lower slope. Brideau et al. (2005) suggested that a large-scale fold may exist, which affects the structural setting of the slide area. The results from the present study agree well and further expand their findings.

A comparison between the orientation of the first-order geological structures and lineaments, and that of the mapped second-order discontinuity sets was performed. A significant agreement was noted between the orientation main lineament trends I, II, and III and the discontinuity set J2, J3, and J1, respectively, as shown in the rosette diagrams (Fig. 11b, c). It is therefore suggested that the structural features mapped at slope scale are strongly correlated to rock mass jointing. The orientation of the geological structures that intersect the slide area, and sub-divide the slide body into blocks (i.e., structures L1, L3, and L4 in Fig. 7), also displays a
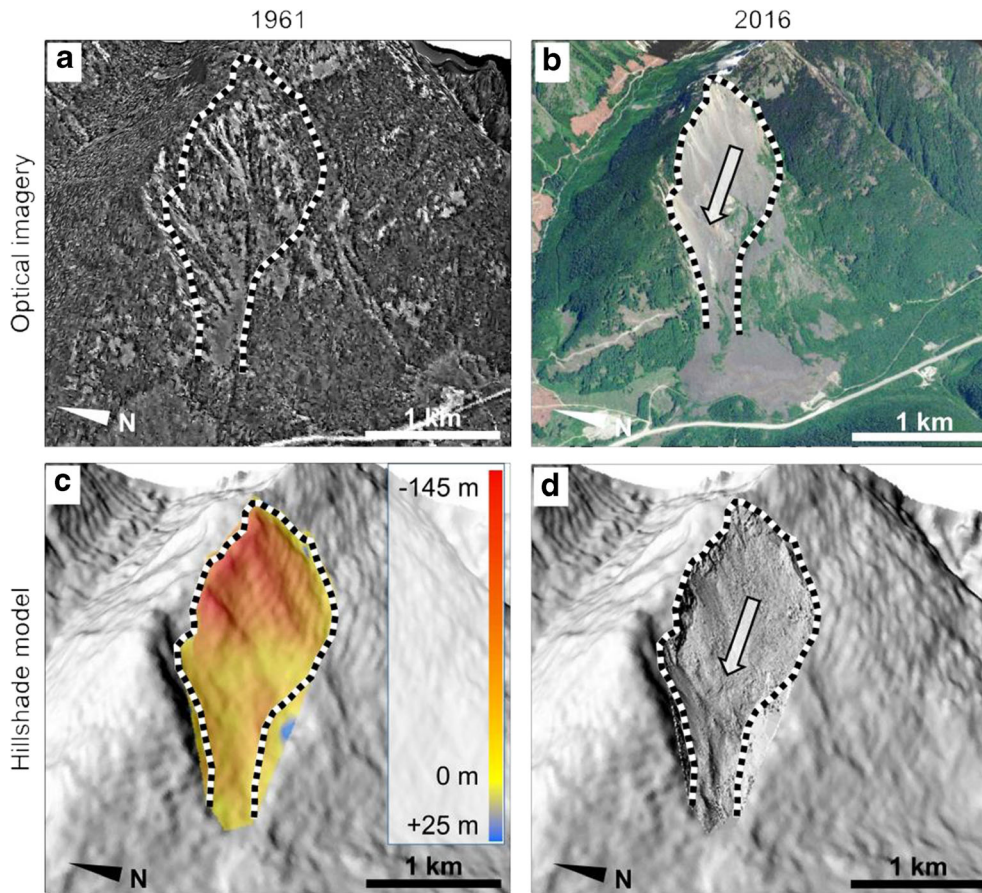
Fig. 10 Comparison between pre-failure and present-day 3D models. a Oblique view of the 1961 SfM point cloud. b Oblique view of the present-day slope from Google Earth (2016 imagery). c Oblique view of the 1961 hillshade SfM model. Color scale shows the elevation loss after the 1965 event. d Hillshade model built by overlaying the 2015 TLS dataset onto the pre-failure SfM topography. Red, dotted curve outlines the 1965 slide area. In the present-day models (b, d), the arrow indicates the inferred displacement direction

general agreement with the orientation of the lineament trends and discontinuity sets, particularly trend I and discontinuity set J2.

Seepage analysis

A seepage investigation was performed using IRT. The FLIR SC7760 thermal camera was employed to capture infrared imagery of the rupture surface from the viewpoint at the southwestern edge of the debris field (Fig. 5). Several seepage areas were identified and mapped, mostly located within the daylighting portion of rupture surface in the central part of the slope (Fig. 12). Most of the seepage was found to occur along discontinuities in set J1 and at lithological contacts between greenstone and felsite. The presence of excessive pore water pressure along discontinuities subparallel to the slope orientation may have decreased the effective stresses along the rupture surface, thus acting as a predisposing factor for the failure. However, the role of groundwater in 1965 is still unclear. Mathews and McTaggart (1969) argued that pore water pressure did not have a primary role in the slope failure, due to the low, below-freezing temperature observed in the area in the weeks prior to the event. In fact, they suggested that freezing temperatures prevented snowmelt, while a continued seepage, due to the geothermal gradient, led to the gradual depletion of hydrostatic pressure in the rock fractures. Conversely, Brideau et al.

(2005) suggested that cold temperature could have caused the groundwater to freeze at the surface, preventing seepage and thus the dissipation of the hydrostatic pressure. In addition, an increase in minimum temperature from −12 to 0 °C was registered at the "Hope A" weather station (located at the Hope Aerodrome) in the two days prior to the failure. This increase in temperature, together with the typically high rainfall in December and January (around 250–280 mm monthly precipitation), may have induced snowmelt and thus a sudden increase in hydrostatic pressure along the rupture surface, possibly triggering the failure.

Rock avalanche deposit block size analysis

The slide deposit was characterized using a SfM approach. Photographs collected with the DJI Phantom 3 Pro Quadcopter were used for the construction of a 3D model and an orthorectified image (Fig. 13a–c). Photographs were obtained by flying the UAV at a constant altitude of 30 m, allowing for a constant ground pixel size of 4 cm throughout the entire image dataset.

A block size analysis distribution was performed on the orthophoto using ArcGIS 10.5. A modified version of the workflow described in Shugar and Clague (2011) was employed. The outline of over 2000 blocks larger than 16 m² was manually digitized and their area computed. The smallest enclosing rectangle was then
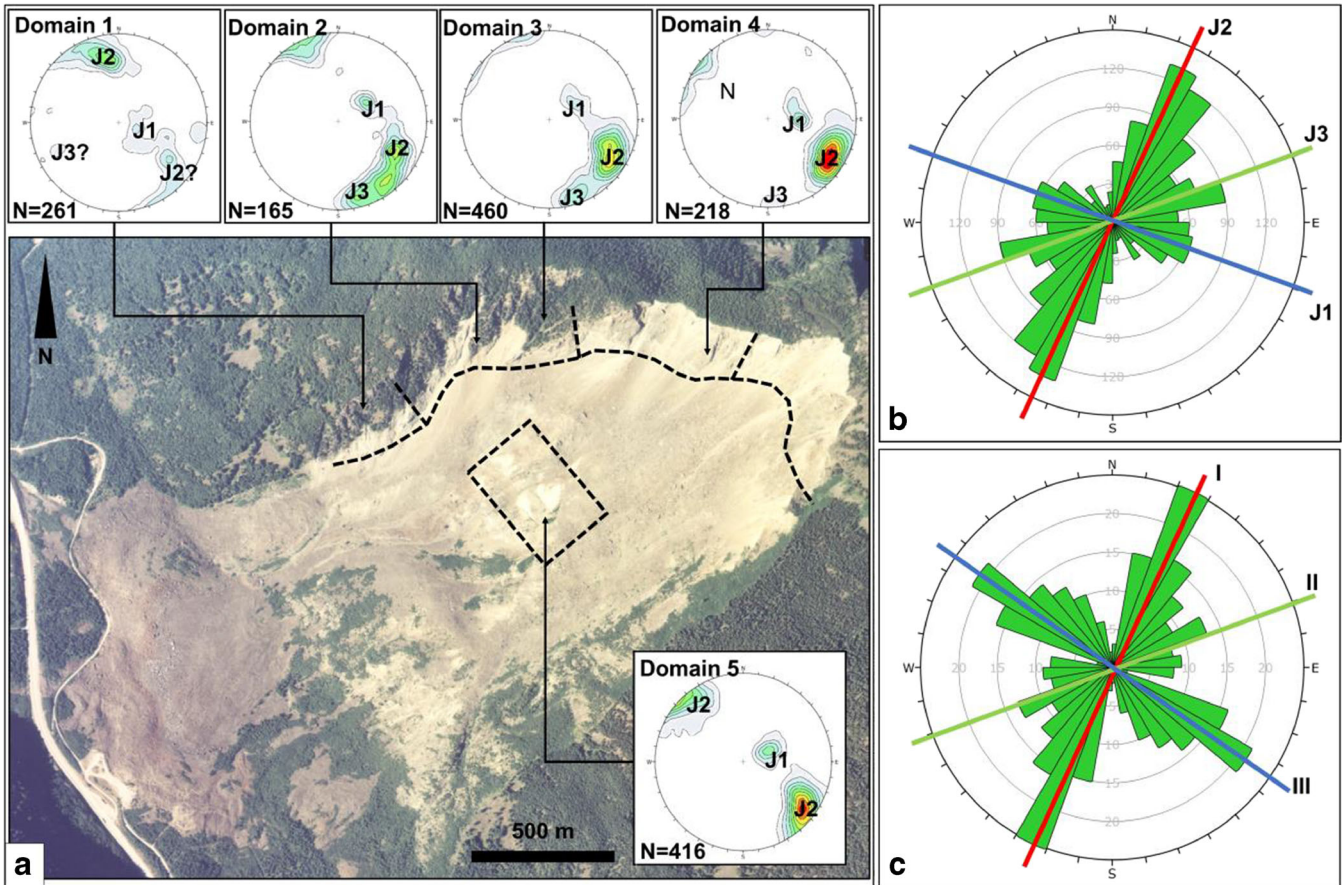
Fig. 11 Overview of the outcrop-scale second order discontinuity mapping performed at the Hope Slide. a Summary of the results from the TDP discontinuity mapping described in Donati et al. (2013). All the stereonets are equal angle, lower hemisphere projections. On the aerial photograph, the dashed lines outline the boundaries of the structural domains derived from the discontinuity mapping (photograph 1996, courtesy of Province of British Columbia, roll BCC96082, frame 19). b Rosette diagram that includes the mapped discontinuities. The orientations of the principal discontinuity sets identified are highlighted. c Rosette diagram obtained from the slope-scale lineaments. Note the similarities with the discontinuity set orientations in (b)
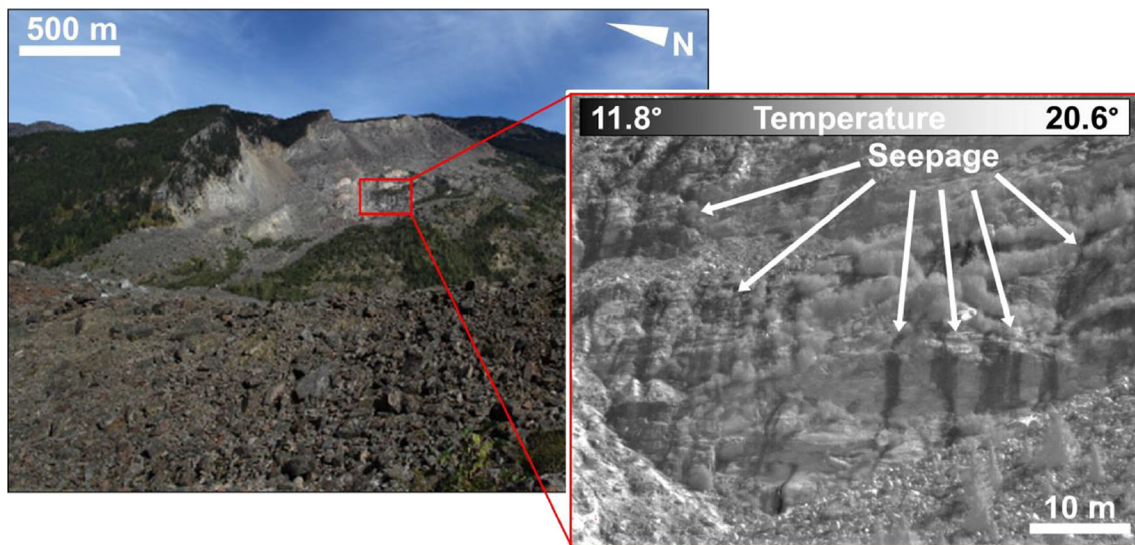

Fig. 12 Example of the thermal imagery collected at the Hope Slide. Darker colors indicate lower temperatures, whereas brighter colors indicate higher temperatures. Low temperatures (10 to 12 °C) identify groundwater seepage from J1 discontinuities and the greenstone/felsite sill contacts. Imagery summer 2016
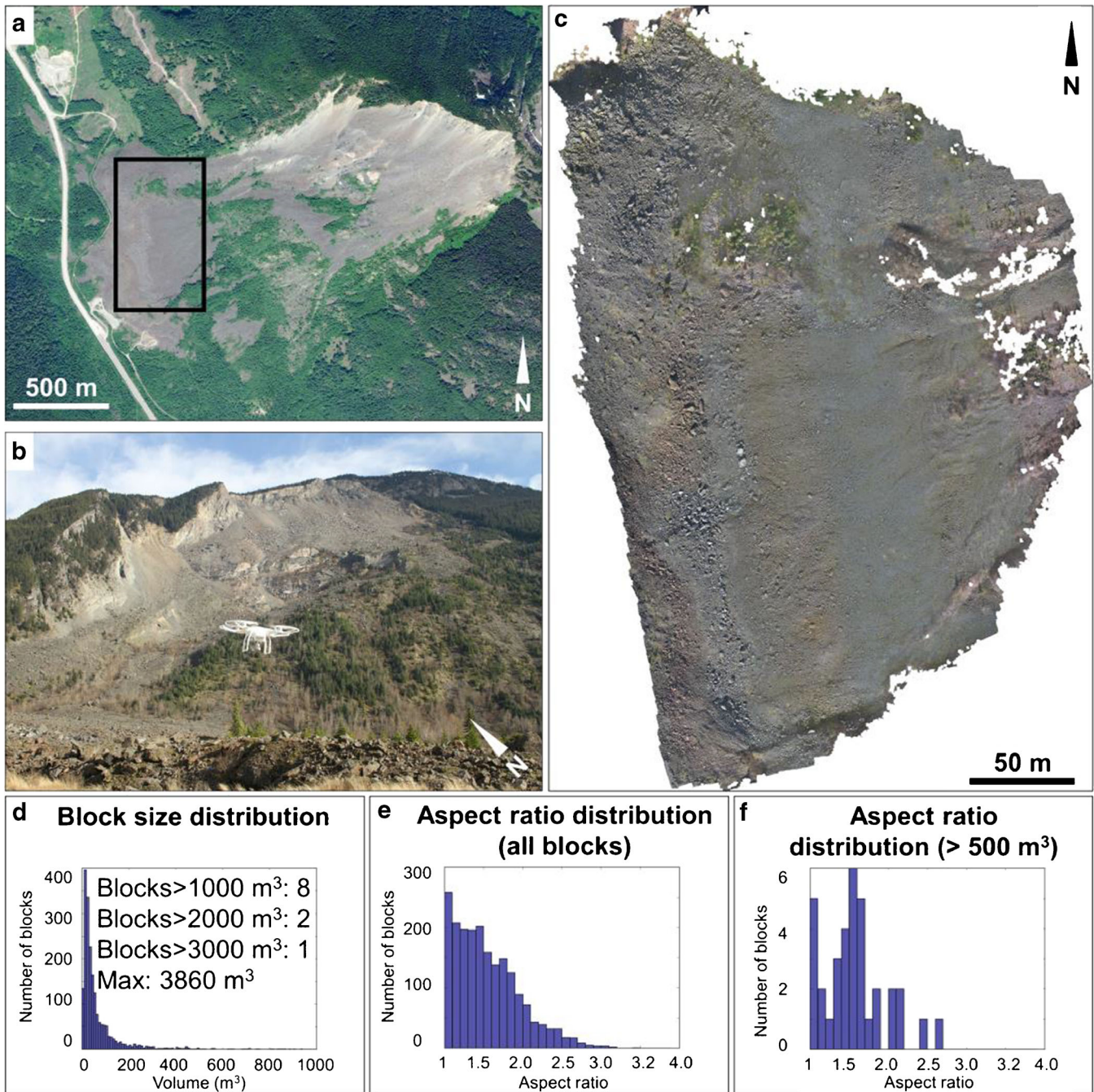
Fig. 13 Summary of the debris characterization at the Hope Slide site. a 2016 Google Earth satellite photograph of the investigated area of the deposit. The polygon shows the location of the investigated area. b The DJI Phantom 3 during the survey (photograph summer 2016). c The orthorectified image of the investigated area. d Block size distribution analysis in the Hope Slide deposit. The maximum block volume computed was 3860 m3. e Aspect ratio distribution for all the digitized blocks. f Aspect ratio distribution for blocks larger than 500 m3

obtained for each of the digitized polygons. The block volume was then estimated as the product of the surface area of the block outlined in the orthophoto and the average side length of the enclosing quadrangle. The maximum estimated block volume within the slide debris is about 4000 m³, while the average volume is 78 m³ (Fig. 13d). For each block, a two-dimensional block aspect ratio was also calculated, defined as the ratio between the length of the major and minor sides of the enclosing rectangle. Aspect ratio

was computed to constrain the relative spacing of each of the discontinuity sets to be considered in the numerical models (see next section). The aspect ratio distribution has a log-normal distribution when all the blocks are considered (Fig. 13e). Conversely, when blocks larger than 500 m³ only are considered, an average aspect ratio of 1.5 is obtained (Fig. 13f). This evidence suggests that while the shape of large blocks may reflect the joint spacing within the intact rock mass, brittle fracturing processes and comminution

due to impacts with other blocks and the ground during the failure cause the original, structurally controlled block shape to be lost. It should be stressed that the purpose of this analysis was not an accurate characterization of the block size distribution representative of the entire deposit, but rather a more general indication of the potential size of the blocks that detached from the slope, prior to any significant comminution.

Numerical modeling

Construction of the 3D numerical model

The results of the present study confirmed the structurally controlled nature of the slide, expanding on the findings from previous works (Brideau et al. 2005; von Sacken 1991). In view of the strong structural control and complex kinematics, the use of a three-dimensional distinct element method (DEM) approach was deemed to be instrumental in simulating realistically the deformation and failure of the Hope Slide.

The three-dimensional simulation of the 1965 Hope Slide was performed using a rigid block approach in 3DEC (Itasca Consulting Group 2016). This assumption allowed to focus on the kinematic behavior of the slide, rather than the role of the internal failure and deformation of individual blocks.

A simplified, pre-failure topography was constructed, which includes the volume that is assumed to have failed during the prehistoric event. The first-order geological structures mapped in the pre-failure geometry were used to subdivide the slope model into the five blocks, B1–B5. The first-order geologic structures are fully persistent in the 3DEC model and represented as cohesionless discontinuities. This assumption was considered adequate because these geological structures are faults with soft gouge (up to 30 cm thick) that had been observed at their core (Brideau et al. 2005). In addition, a planar basal rupture surface was created, parallel to the discontinuity set J1. The rupture surface in the model intersects the daylighting portion of sliding surface visible in the central part of the slide area. Brideau et al. (2005) suggested that the slide may have moved along a stepped sliding surface; however, in this numerical analysis, a step-path failure surface morphology has not been implemented, as the true morphology of the rupture surface is largely not visible due to the debris cover.

The second-order geological structures (i.e., discontinuity sets) were implemented in the model by considering both the results of the rock mass characterization and the debris block size analysis. The average orientation of the discontinuity sets was obtained from TDP mapping of the lateral scarp and upper headscarp. The spacing of each discontinuity set was based on the aspect ratio of the largest blocks digitized in the orthorectified photograph of the debris. The ratio between the spacing of each discontinuity set was maintained equal to the 2D aspect ratio of the largest blocks mapped in the orthophoto. In other words, as J3 and J2 have the wider and the closest discontinuity spacing, respectively (as determined from the virtual scanline mapping), a ratio of 1.5, equal to the average aspect ratio for larger blocks, was maintained in the numerical model between the spacing of J3 and J2. Similarly, a ratio of 1.25 was maintained between the spacing of J3 and J1. These simulations were conducted, using a constant discontinuity set spacing ratio, while varying the block volume. This approach allowed the potential, initial block size that may have characterized the slide mass at the onset of failure, and prior

to any comminution, to be considered. It should be noted that considering spacing values obtained directly from the virtual scanline mapping ignores the presence of rock bridges along discontinuity planes, causing the block size to be underestimated and the slide volume to consist of blocks much smaller than those visible in the deposit. A similar approach was employed in Spreafico et al. (2016). A block size of 80,000 m^3 (20 times the maximum block size observed in the debris) was used for model 1, 40,000 m^3 for model 2 (10 times the maximum block size), and 20,000 m^3 for model 3 (5 times the maximum block size). Material density and discontinuity strength parameters were assigned following geotechnical laboratory test results and estimates described in von Sacken (1991) and Brideau et al. (2005) (Table 2). A water table was not implemented in these 3D model simulations and the slope was assumed to be dry. The sides and the base of the 3D model were fixed and any lateral displacement prevented.

The model was initially run with high discontinuity strength parameters, to allow stresses to be correctly computed along the joints, preventing the global failure of the slope, and avoiding shock loading of the model. Block B1 and block B2 were then deleted from the model, simulating the occurrence of the prehistoric rockslide and the resulting debuttressing effect in the upper slope. After equilibrium was achieved in the 3DEC model (i.e., based on unbalanced force in the model), discontinuities were assigned the parameters obtained from laboratory tests (or based on literature data). Finally, the cohesion of the rupture surface was gradually reduced in 0.02 MPa increments at each simulation stage, until the failure of slide blocks B4 and B5 was simulated. Each stage was considered complete when a new equilibrium condition was achieved. This incremental strength reduction is to approximate a progressive slope failure due to failure of rock bridge and strain softening due to static (creep and fatigue) and cyclic loading (seismic, freeze–thaw, and seasonal groundwater variation).

Table 2 Summary of the properties used for the numerical simulation of the 1965 Hope Slide (residual values are shown in parentheses)

Rock mass			
Material 1			
Density	2850 kg/m^3		
Constitutive model	Rigid blocks		
Discontinuities			
	Rupture surface	**J1, J2, J3**	**First-order structures**
Friction angle (°)	28 (20)	28 (2-0)	24 (18)
Cohesion (MPa)	1.5 (0)*	2.5 (0)	0
Tensile strength (MPa)	0	0.2 (0)	0
Normal/shear stiffness (GPa/m)	10/1	10/1	10/1

*Peak cohesion value was progressively decreased until 3DEC slope failure was simulated

Numerical modeling results

Three-dimensional numerical modeling of the Hope Slide realistically simulated the 1965 slope failure in two stages as observed on site. The numerical results show that the block size affects the stability of the slope. When larger block sizes are considered (10 and 20 times the largest block observed in the debris), a two-stage failure is simulated (Fig. 14a, b), in which the failure of the slide block B4 occurs for higher cohesion values, compared with the slide block B5. In model 2, the numerical displacement rate of block B5 immediately after the detachment of slide block B4 (400,000 numerical time steps) is relatively low, possibly due to the interlocking of individual joint bounded blocks. As the individual blocks become kinematically free, the numerical displacement rate increases (Fig. 14b). The joint bounded block comprising the history point of slide block B4 acquired full kinematic freedom after 900,000 numerical time steps, as indicated by the steepening of the numerical displacement versus numerical time step curve (Fig. 14b). The curve flattens when the joint bounded block comprising the history point reaches the deposit (Fig. 14a, b). No obvious block interlocking has been observed during the failure of slide block B5. When a smaller block size (five times the largest block) is used in model 3, the failure occurs in a single stage, and the displacement rates within the slide blocks B4 and B5 increase at the same time (Fig. 14c). Table 3 summarizes the cohesion magnitudes at which the failure of slide blocks B4 and B5 was simulated.

Discussion

Interpretation of the Hope Slide based on slope kinematics

Characterization of the Hope Slide conducted using the new methods and collected data from this research has provided important insight into the evolution of the slope before and after the 1965 failure. It has been previously suggested that the prehistoric slope failure caused the removal in the lower part of the slope of a volume of rock similar to the 1965 slide (Mathews and McTaggart 1969). In contrast, the material removed during the 1965 event originated predominantly from the upper slope.

The prehistoric event is suggested to have had an important role in the 1965 rockslide. Block theory analysis indicates that the prehistoric event caused removal of a key block and propagation of the instability due to reduced kinematic restraint on the upper blocks. The event occurred approximately 9700 years B.P., shortly after the disappearance of the Pleistocene Cordilleran Ice Sheet, about 10,000 years B.P. (Clague et al. 1983). In view of its low elevation, it is likely that the Johnson Ridge was completely overtopped by the ice sheet, as hypothesized by Waddington (1995). The prehistoric slide was probably induced by removal of support following glacial retreat and fluvial erosion at the base of the slope. The relation between the retreat of Holocene glaciers and slope stability has been described for both recent and historic events (Clayton et al. 2017; Roberti et al. 2018). In fact, long-term glacial history also affects present-day slope stability. Cruden and Hu (1993) suggest that an "exhaustion" process may condition rock slopes for failures even thousands of years after glacial retreat or rapid fluvial incision. Riva et al. (2018) modeled the long-term deformation of a rock slope previously buttressed by a glacier and observed that the accumulation of internal damage can progress for long periods of time (>15,000 years) in sagging rock slopes.

Eberhardt et al. (2004) and Leith (2012) similarly show, using numerical models, that the removal of glacier resulted in damage at the toe of the 1991 Randa rockslide. It is suggested that a large slope failure may result in progressive internal damage, and that the 1965 Hope Slide may represent the final stage of an extremely slow slope degradation and weakening process that started with the prehistoric failure. We suggest that after such a slope toe failure, a long-term deformation initiated in the upper slope, inducing the formation and accumulation of slope damage both within the slide volume, in the form of tension cracks, counterscarps (as those visible in the pre-failure aerial imagery), and rock mass dilation, and more importantly along the rupture surface, through gradual failure of rock bridges and sub-critical crack propagation (Atkinson 1984), until failure occurred. This hypothesis agrees with the findings of Evans and Couture (2002). Table 4 summarizes conceptually the proposed mechanism, focusing on the slope damage that may have characterized the slope throughout the different stages of its geomorphic evolution.

The remote sensing and numerical modeling analyses show that, from a kinematic perspective, the two main blocks that failed during the 1965 event were characterized by a substantially different displacement behavior. The slide block B4, bounded by the first-order structures L3 and L6, probably slid along a basal surface parallel to the slope and discontinuity set J1. This configuration indicates a planar sliding mechanism, with displacement occurring in a 248° direction (Fig. 15). Slide block B5 may have been initially buttressed by slide block B4. The failure of slide block B4, then, caused the instability to propagate toward slide block B5. This block, however, does not appear to have failed through a planar sliding mechanism: the presence along the lower boundary of the first-order structure L2 may have led instead to a translational wedge failure, with displacement in a 291° direction (along the intersection with the basal surface; Fig. 15). Brideau et al. (2005) observed that most of the failure material accumulated in the northwestern part of the deposit, and that the slide material largely traveled in a westerly direction. This observation appears to agree well with a sliding direction partially controlled by L2, and a wedge failure mechanism for the largest slide block involved in the 1965 event and is also supported by the numerical modeling results. In the 3DEC model simulation, the occurrence of a two-stage failure varies due to the different kinematic conditions between slide blocks B4 and B5 at model scale. It was observed that the failure of slide block B4 occurs as a result of a purely planar sliding along the rupture surface (i.e., discontinuity set J1). The trend/plunge of the sliding direction is $32°/248°$, and the lateral release surfaces are provided by the first-order structures L6 and L3. This kinematic setting is also reproduced in the models at the element scale, where sliding of individual joint bounded blocks occurs along discontinuity set J1, with J2 and J3 acting as lateral release surfaces. As a result, at both model and element scales, the shear strength is only mobilized along the J1 planes. At the element scale, the tensile strength (lower in magnitude, compared with the shear strength) is implicitly provided by intact rock bridges and is mobilized along J2 and J3. In contrast, failure of slide block B5 kinematically resembles a wedge failure at the model scale. The intersection between the basal surface and structure L2 causes sliding along a plunge/trend of 24°/291°. At the element scale, the individual joint bonded blocks slide along J1 and J3, causing the mobilization of the shear strength on both joint sets. The trend and plunge of the
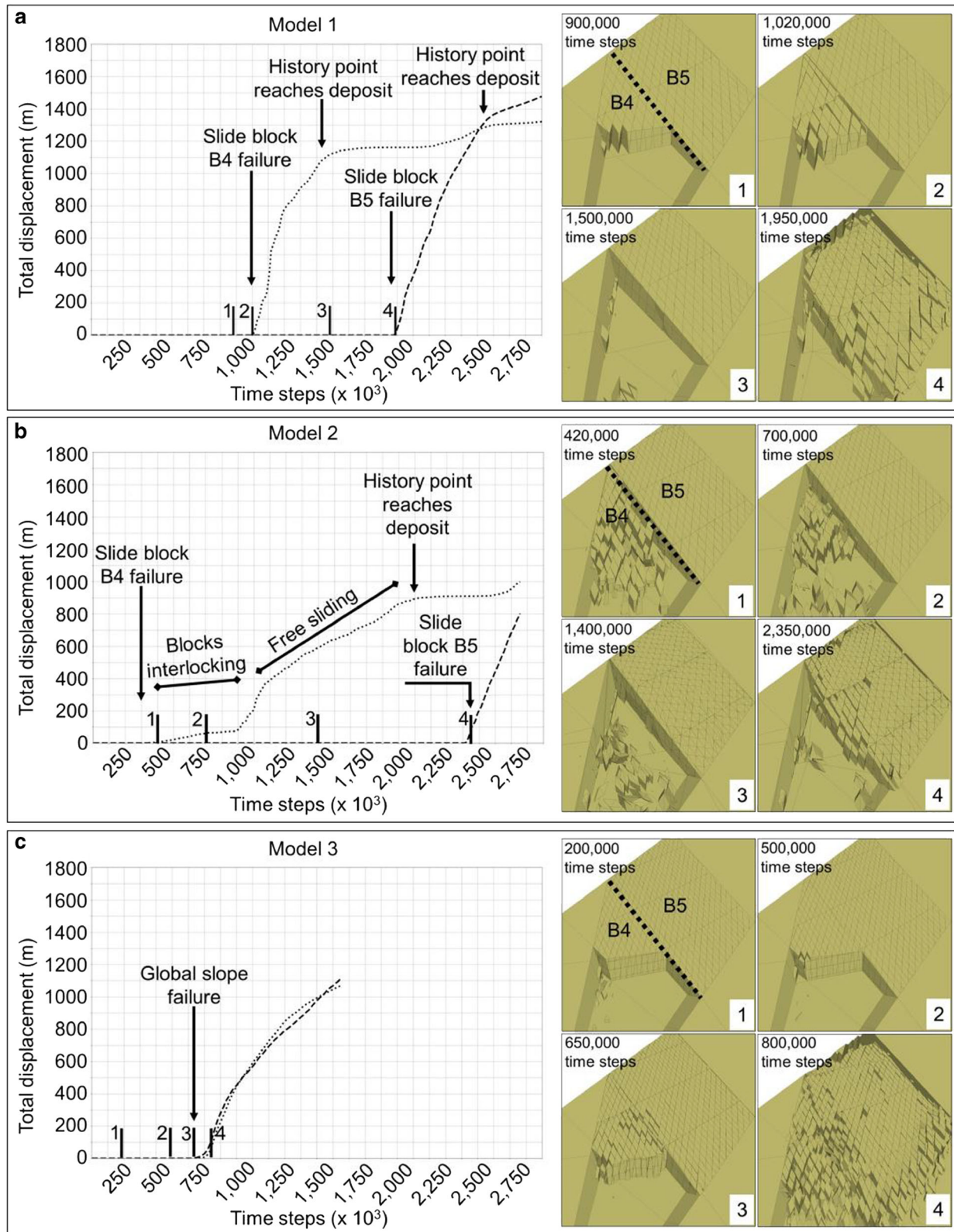
Fig. 14 Summary of the numerical modeling of the 1965 Hope Slide using 3DEC. Dotted and dashed curves display total displacement magnitude of history points in slide blocks 4 and 5, respectively. a Model 1 (block size 20× largest block in landslide deposit). Plots 1–4 show block displacements for increasing numerical time steps. b Model 2 (block size 10× largest block in landslide deposit). c Model 3 (block size 5× largest block in landslide deposit). The failure of both slide block 4 (dotted curve) and slide block 5 (dashed curve) was simulated at the same time

Table 3 Rupture surface cohesion value at failure in 3DEC models (in brackets, the percentage of decrease from the original value is reported)

	Assumed block size (m³)	Slide block B4 rupture surface cohesion at failure (MPa)	Slide block B5 rupture surface cohesion at failure (MPa)
Model 1	80,000	0.98 (−34.7%)	0.92 (−38.6%)
Model 2	40,000	1.12 (−25.3%)	1.02 (−32.0%)
Model 3	20,000	1.10 (−26.6%)	1.10 (−26.6%)

line of intersection, i.e., the sliding direction, is 31°/263°. Discontinuity set J2 within slide block B5 acts as a rear release surface, and the tensile strength is therefore mobilized along this discontinuity set only (Fig. 15).

The numerical model results suggest that the slide block B4 acted as key block in the 1965 Hope Slide failure, its removal providing kinematic freedom for slide block B5 to displace. According to this interpretation, the first-order geological structure L2 plays a critical role in the evolution and progression of the failure. The slope below this structure was not involved in the 1965 Hope Slide failure and may have acted as a buttress, resulting in the development of the wedge failure mechanism.

Comparison with previous studies

Since the occurrence of the Hope Slide, in 1965, several studies have been undertaken, which have progressively enhanced our understanding of the mechanisms underlying the failure. Anderson (1965) compiled a comprehensive timetable of the event, based on witnesses' accounts. His work, although not strictly a geological investigation, provides an overview of the environmental conditions that existed at the site in the days and hours before the slide occurred. The first geological investigation is described by Mathews and McTaggart (1969, 1978). Their work represents the first significant appraisal of the landslide, in terms of lithological factors, involved volume, and long-term evolution of the slope. Bruce and Cruden (1977) presented the first limit equilibrium analysis of the Hope Slide, using direct shear tests to constrain input data. Von Sacken (1991) performed and described the first extensive field work focused on the structural characterization of the slope, highlighting for the first time the important role of geological structures on the slide evolution. She also suggested for the first time that the Hope Slide might have occurred in two stages, instead of a single event, preceded by a snow avalanche, as reported in Anderson (1965), and highlighted the presence of sackung-type features in the upper slope. The hypothesis of a long-term slope deformation prior to the failure was later substantiated by field work and trenching undertaken by Evans and Couture (2002). Brideau et al. (2005) further investigated the structural control on the Hope Slide, highlighting the correlation between rock mass damage and proximity to slope-scale geological structures, and noting the presence of gouge at the core of major faults. They also produced the first three-dimensional conceptual model of the Hope Slide, which included the principal features controlling the slope stability (faults, shear zones, lithological contacts, rock mass jointing). The findings we have presented in the present study build upon and agree with the observations and results described above. Furthermore, we provide a new and enhanced insight on the long-term evolution and the control of structural geology factors on the Hope Slide. We use, for the first time at this site, multiple remote sensing techniques crucial in investigating the inaccessible parts of the scarps. Together, historical and new data showed that slope kinematics, and especially its evolution, was a critical factor in defining the behavior of the slide both during the failure and since the original post-glacial retreat triggered slope failure. The three-dimensional distinct element modeling was instrumental in realistically simulating the failure and demonstrated that structurally controlled failures such as the Hope Slide cannot be adequately investigated using two-dimensional approaches alone, which tend to oversimplify and often ignore the kinematics of the true failure mechanism.

Scale effects in numerical modeling

The role of scale and scale effects on numerical models is of major importance in slope stability analyses. The effects of a change in block size (and thus, in discontinuity spacing) on the failure mechanism has been investigated by several authors. Hencher et al. (1996) employed a physical–numerical modeling approach to conceptually investigate the failure of open pit slopes and underground excavations. Using base-friction physical models, they noted that, when the same discontinuity orientation, persistence, and relative set spacing is maintained, the slope failure mechanism was strongly controlled by the size of the blocks composing the slope. A simulated slope constituted by very small block was noted to be affected by a shallow translational slide. As the block size increased (together with discontinuity spacing), the failure mechanism progressively switched to a planar sliding and then to a toppling failure. Using a 2D continuum numerical modeling approach, Hammah et al. (2007) also investigated the effect of joint persistence and block size on the failure mechanism and strength of conceptual rock slopes constituted by jointed rock masses. The progressive decrease in discontinuity persistence and block size caused the slope failure mechanism to progressively change from planar sliding to a pseudo-rototranslational failure, typical of weak, heavily fractured rock masses. Using a 3D distinct element numerical modeling approach, Corkum and Martin (2004) analyzed the effects of block size on the stability and kinematic freedom of the Block 731, a stabilized rock slope near the abutment of the Revelstoke Dam (British Columbia, Canada). They noted that the block size, and in turn the number of blocks, selected for the simulation strongly affected the stability and evolution of the simulated slope. Using the same modeling approach, Brideau and Stead (2010) studied the effects of block shape, discontinuity orientation on the slope failure mechanism. They noted that the style and volume of the failure are affected by changes in the orientation of the basal, lateral, and rear release surfaces affected, as well as the kinematic confinement of the simulated slope. Sitar et al. (2005) employed a discontinuous deformation analysis to study the effects of block size and block number in a numerical model of the Vajont Landslide, and noted that the velocity and kinematic freedom of the slide increased together with the number of blocks considered in the simulation. They concluded that the progressive disintegration and fracturing

Table 4 Conceptual evolution of the slope damage at the Hope Slide (sketches describe conceptually the evolution of the Hope Slide since initiation of the instability after glaciation)

|	Conceptual sketch	Geomorphic conditions	Slope damage evolution
Stage 1		• Ice-covered valley • Buttressed slope • Slopes over-steepened by glacier advance	• Tension cracks, counterscarps formed during previous stages of glacial retreat • Fractures possibly propagated in sub-critical conditions during previous stages of glacial retreat and advance
Stage 2		• Glacial retreat • Slope deformation initiates; the boundaries of the deforming slope are structurally controlled	• Tension cracks, counterscarps, and scarps extend to the boundary of the unstable area • Freeze-thaw cycles causes opening and propagation of fractures • Brittle fracturing initiates the formation of a continuous rupture surface • Bulging causes dilation and rock mass damage at the toe
Stage 3		• Prehistoric failure. Key-block removed (slide blocks B1 and B2) • Valley floor filled with debris and raised by tens of meters • Initiation of slow deformation due to stress redistribution in the upper slope	• A steep, sharp headscarp forms as a result of the failure • Syn-failure cracks due to stress relaxation form behind the headscarp • Stress relaxation causes propagation of fractures in the volume not involved in the failure
Stage 4		• Prehistoric headscarp "smoothed" and eroded • Eroded material forms a debris fan at the base of the slope • Blocks from rockfall source areas deposit in the accumulation surfaces along the slope	• Counterscarps form in the upper part of the unstable area, due to slow, progressive slope creep • Freeze-thaw cycles cause opening and propagation of fractures • Brittle fracturing of rock bridges between non-persistent discontinuities leads to the formation of a continuous rupture surface in the upper slope • Increasing weathering and alteration at the base of the debuttressed blocks enhance cliff erosion and the rock mass damage
Stage 5		• Upper slope collapses in two stages (slide blocks B4 and B5) • Slide material obliterates the debris fan and the Outram Lake at the base of the slope	• Localized instability at the edges of the slide area • Opening of a tension crack behind the headscarp • Freeze-thaw cycles cause opening and propagation of fractures • Localized accumulation of rock mass damage within areas undergoing deformation along the headscarp
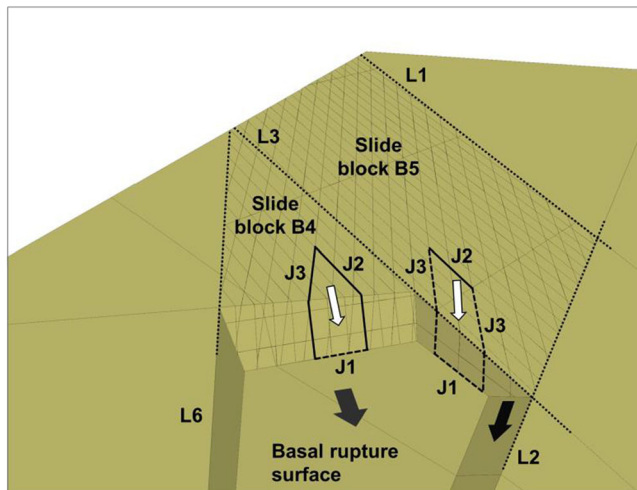
Fig. 15 Kinematics of the Hope Slide blocks at large and small scale. At model scale, the slide block B4 acts as key block for the failure of the slide block B5. Black arrows indicate the displacement direction of the slide blocks. Slide block B4 is kinematically free to slide along the basal rupture surface. Slide block B5 slides along the basal rupture surface and L2, with the latter kinematically constraining the block along the lower side. At the element scale, the stability of the individual joint bounded blocks forming slide block B4 is governed by the shear strength (dashed traces) along J1 and the tensile strength (solid traces) along J2 and J3. In slide block B5, only J2 fails in tension, while shear strength controls sliding along J1 and J3. White arrows indicate the sliding direction of the individual joint bounded blocks

is an important factor that should be kept into consideration in the analysis of large rockslides.

In the present paper, the results of the numerical modeling confirmed the important relation between the size of the simulated blocks and the behavior of the slope. The size of the simulated blocks affected the evolution of the slope, as it controlled the occurrence of a single-event failure (using a smaller block size) or a two-stage failure (when larger blocks were considered). In the simulated models, the change in block size in the investigated model did not affect the failure mechanism; however, it did significantly affect the overall strength of the slope. The model constituted by larger blocks remains stable for lower values of cohesion, compared with one constituted by smaller blocks. This observation has potentially significant implications for back-analysis stability studies, as the back-calculated shear strength of the rupture surface appears to be strictly correlated to the model geometry and block size, even if the same failure mechanism is simulated.

Conclusions

The Hope Slide, one of the largest historical rock avalanches in Canada, occurred as two events in the early morning of January 9, 1965. The slope had been affected by a prehistoric slope failure, which had left a clearly visible scar in the topography and a 60-m-thick deposit at the bottom of the valley.

In the present study, we highlighted the important role of tectonic structures on the behavior and evolution of the 1965 Hope Slide. We observed that the tectonic structures that controlled the 1965 slide also appeared to control the location of the prehistoric

event. Although the occurrence of the prehistoric instability has been recognized by several authors prior to the 1965 failure, its effects on the kinematics of the remaining slope had not been addressed in detail. It is suggested in this research that the prehistoric slope failure caused the removal of a key block from the lower slope, thus initiating a long-term slope deformation that eventually led to the 1965 Hope Slide.

We suggest that in order to reconstruct the evolution of the stability and geomorphic evolution of a rock slope, a detailed slope characterization is required. The objective of the slope investigation should be to characterize large, first-order structures that govern the global behavior of the slope, and the lower order features (e.g., joints, block size) that are critical in defining the slope kinematics and the mechanical strength of the rock mass. This research highlights that the stability of rock slopes is not only strongly influenced by slope kinematics but also by the geomorphic and geomechanical evolution of the slope with time. Glacial retreat, oversteepening, and removal of key blocks from the slope may initiate a progressive failure process. Gradual weakening of the slope is accompanied by the formation of internal and external rock slope damage features, which may enhance kinematic freedom within the slope, potentially leading to major rockslides. It is therefore suggested that a three-dimensional slope kinematics and damage investigation should be a required component in any major rock slope characterization, and that the potential evolution of kinematic freedom should be addressed to realistically assess the long-term stability of large rock slopes.

Compliance with ethical standards

Conflict of interest The authors declare that they have no conflict of interest.

References

AdamTechnology (2017) 3DM Analyst Mine Mapping Suite 2.5 and User's Manual

Agisoft LLC (2018) Photoscan 1.4 and User's Manual

Agliardi F, Crosta GB, Frattini P (2012) Slow rock-slope deformation. In: Clague JJ, Stead D (eds) Landslides: types, mechanisms and modeling. Cambridge University Press, pp 207–221

Ambrosi C, Crosta GB (2006) Large sackung along major tectonic features in the Central Italian Alps. Eng Geol 83(1-3):183–200. https://doi.org/10.1016/j.enggeo.2005.06.031

Anderson FW (1965) The Hope Slide story. Frontiers Unlimited, Calgary

Atkinson BK (1984) Subcritical crack growth in geological materials. J Geophys Res B Solid Earth 89(B6):4077–4114. https://doi.org/10.1029/JB089iB06p04077

Azzoni A, Chiesa S, Frassoni A, Govi M (1992) The Valpola landslide. Eng Geol 33(1):59–70. https://doi.org/10.1016/0013-7952(92)90035-W

Birch J (2006) Using 3DM Analyst mine mapping suite for rock face characterisation. In: Tonon F, Kottenstette J (eds) Laser and photogrammetric methods for rock face characterization. Workshop at ARMA 2006. Golden, CO. June 17-18. pp. 13–32.

Brideau MA (2010) Three-dimensional kinematic controls on rock slope stability conditions. Ph.D. Thesis, Simon Fraser University

Brideau MA, Stead D (2010) Controls on block toppling using a three-dimensional distinct element approach. Rock Mech Rock Eng 43(3):241–260. https://doi.org/10.1007/s00603-009-0052-2

Brideau MA, Stead D, Kinakin D, Fecova K (2005) Influence of tectonic structures on the Hope Slide, British Columbia, Canada. Eng Geol 80(3–4):242–259. https://doi.org/10.1016/j.enggeo.2005.05.004

Bruce I, Cruden D (1977) The dynamics of the Hope Slide. Bull Int Assoc Eng Geol 16:94–98

Cairnes CE (1924). Coquihalla Area, British Columbia. Geological Survey of Canada, Gelogical series 119. Memoir no. 139. https://doi.org/10.4095/100855

Clague JJ, Luternauer JL, Hebda RJ (1983) Sedimentary environments and postglacial history of the Fraser Delta and lower Fraser Valley, British Columbia. Can J Earth Sci 20(8):1314–1326. https://doi.org/10.1139/e83-116

Clayton A, Stead D, Kinakin D, Wolter A (2017) Engineering geomorphological interpretation of the Mitchell Creek Landslide, British Columbia, Canada. Landslides 14(5):1655–1675. https://doi.org/10.1007/s10346-017-0811-1

CloudCompare 2.10 (2019) CloudCompare 2.10 [GPL software] – retrieved from http://www.cloudcompare.org/. Accessed 10 Jul 2019

Corkum AG, Martin CD (2004) Analysis of a rock slide stabilized with a toe-berm: a case study in British Columbia, Canada. Int J Rock Mech Min Sci 41(7):1109–1121. https://doi.org/10.1016/j.ijrmms.2004.04.008

Cruden D, Hu X (1993) Exhaustion and steady state models for predicting landslide hazards in the Canadian Rocky Mountains. Geomorphology 8(4):279–285. https://doi.org/10.1016/0169-555X(93)90024-V

Cundall PA (2011) Lattice method for modeling brittle, jointed rock. In: Sainsbury D, Hart R, Detournay C, Nelson M (eds) Continuum and distinct element numerical modeling in geomechanics. Proceedings of the 2nd International FLAC/DEM Symposium. 14–16 February, Melbourne, Australia

Donati D, Stead D, Ghirotti M, Wolter A (2013) A structural investigation of the Hope Slide, British Columbia, using terrestrial photogrammetry and rock mass characterization. Rend Online Soc Geol Ital 24:107–109 (in Italian)

Donati D, Stead D, Brideau MA, Ghirotti M (2017) A remote sensing approach for the derivation of numerical modelling input data: insights from the Hope Slide, Canada. In: SAIMM (ed). 'Rock Mechanics for Africa' AfriRock Conference 2017. Proceedings of the ISRM International Symposium. October 2–7, Cape Town, South Africa, Paper AR-47

Donati D, Stead D, Onsel E (2018) New approaches to characterize brittle fracture and damage in fractured rock masses. In: Proceedings of the 10th Asian Rock Mechanics Symposium (ARMS10). The ISRM International Symposium for 2018. October 29-November 3, Singapore

Donati D, Stead D, Elmo D, Borgatti L (2019) A preliminary investigation on the role of brittle fracture in the kinematics of the 2014 San Leo Landslide. Geosciences 9(6):256. https://doi.org/10.3390/geosciences9060256

Donati D, Stead D, Stewart T, Marsh J (2020) Numerical modelling of slope damage in large, slowly moving rockslides: insights from the Downie Slide, British Columbia, Canada. Eng Geol 273:105693. https://doi.org/10.1016/j.enggeo.2020.105693

Eberhardt E, Stead D, Coggan JS (2004) Numerical analysis of initiation and progressive failure in natural rock slopes—the 1991 Randa rockslide. Int J Rock Mech Min Sci 41(1):69–87. https://doi.org/10.1016/S1365-1609(03)00076-5

ESRI (2017) ArcGIS 10.5. https://www.esri.com/. Accessed 1 Oct 2017

Evans SG, Couture R (2002) The 1965 Hope Slide, British Columbia; catastrophic failure of a sagging rock slope. In: 2002 Annual Meeting of the Geological Society of America. October 27–30, Denver, CO. Paper No. 16-6.

FLIR Systems Inc (2015) ResearchIR 4. https://www.flir.ca/products/researchir/. Accessed 1 Sept 2015

Francioni M, Stead D, Clague JJ, Westin A (2018) Identification and analysis of large paleo-landslides at Mount Burnaby, British Columbia. Environ Eng Geosci 24(2):221–235. https://doi.org/10.2113/EEG-1955

Francioni M, Simone M, Stead D, Sciarra N, Mataloni G, Calamita F (2019) A new fast and low-cost photogrammetry method for the engineering characterization of rock slopes. Remote Sens 11(11):1267. https://doi.org/10.3390/rs11111267

Ganerød GV, Grøneng G, Rønning JS, Dalsegg E, Elvebakk H, Tønnesen JF, Kveldsvik V, Eiken T, Blikra LH, Braathen A (2008) Geological model of the Åknes rockslide, western Norway. Eng Geol 102 (1–2):1–18. https://doi.org/10.1016/j.enggeo.2008.01.018

Gischig VS, Eberhardt E, Moore JR, Hungr O (2015) On the seismic response of deep-seated rock slope instabilities — insights from numerical modeling. Eng Geol 193:1–18. https://doi.org/10.1016/j.enggeo.2015.04.003

Goodman RE, Shi G (1985) Block theory and its application to rock engineering. Prentice-Hall, Englewood Cliffs

Grøneng G, Lu M, Nilsen B, Jenssen AK (2010) Modelling of time-dependent behavior of the basal sliding surface of the Åknes rockslide area in western Norway. Eng Geol 114(3–4):414–422. https://doi.org/10.1016/j.enggeo.2010.05.017

Guerin A, Jaboyedoff M, Collins BD, Derron MH, Stock GM, Matasci B, Boesiger M, Lefeuvre C, Podladchikov YY (2019) Detection of rock bridges by infrared thermal imaging and modeling. Sci Rep 9:1–19. https://doi.org/10.1038/s41598-019-49336-1

Hammah R, Yacoub T, Curran JH (2007) Variation of failure mechanisms of slopes in jointed rock masses with changing scale. www.rocscience.com. Accessed 1 May 2020

Havaej M, Coggan J, Stead D, Elmo D (2016) A combined remote sensing–numerical modelling approach to the stability analysis of Delabole Slate Quarry, Cornwall, UK. Rock Mech Rock Eng 49(4):1227–1245. https://doi.org/10.1007/s00603-015-0805-z

Hencher SR, Liao Q-H, Monaghan BG (1996) Modelling slope behavior for open-pits. Trans Inst Min Metall Sect A 105:A37–A47

Hosseini F, Pichierri M, Eppler J, Rabus B (2018) Staring spotlight TerraSAR-X SAR interferometry for identification and monitoring of small-scale landslide deformation. Remote Sens 10(6):1–18. https://doi.org/10.3390/rs10060844

Humair F, Pedrazzini A, Epard JL, Froese CR, Jaboyedoff M (2013) Structural characterization of Turtle Mountain anticline (Alberta, Canada) and impact on rock slope failure. Tectonophysics 605:133–148. https://doi.org/10.1016/j.tecto.2013.04.029

Hungr O, Amann F (2011) Limit equilibrium of asymmetric laterally constrained rockslides. Int J Rock Mech Min Sci 48(5):748–758. https://doi.org/10.1016/j.ijrmms.2011.04.008

Itasca Consulting Group (2016) 3DEC 5.2 and User's manual.

Jaboyedoff M, Derron M-H (2020) Landslide analysis using laser scanners. In: Tarolli P, Mudd SM (eds): Remote Sensing of Geomorphology. Development in Earth Surface Processes book series 23:207–230. https://doi.org/10.1016/B978-0-444-64177-9.00007-2

Leith KJ (2012) Stress development and geomechanical controls on the geomorphic evolution of alpine valleys. Ph.D. Thesis, ETH Zurich. https://doi.org/10.3929/ethz-a-007597326

Lu H, Fredlund MD, Chaudhary KB, Lu H, Fredlund MD (2016) Comparison of 3-D limit equilibrium methods. In: GeoVancouver 2016. Proceedings of 69th Canadian Geotechnical Society Conference. October 2–5, Vancouver, Canada 2016. Paper 3746.

Mathews WH, McTaggart KC (1969) The Hope Landslide, British Columbia. Proc Geol Assoc Can 20:65–75

Mathews WH, McTaggart KC (1978) Hope Rockslides, British Columbia, Canada. In: Voight B (ed) Rockslides and avalanches, 1. Elsevier, London, pp 259–275

McTaggart KC, Thompson RM (1967) Geology of part of the Northern Cascades in Southern British Columbia. Can J Earth Sci 4(6):1199–1228. https://doi.org/10.1139/e67-081

Munjiza A, Owen DRJ, Bicanic N (1995) A combined finite-discrete element method in transient dynamics of fracturing solids. Eng Comput 12(2):145–174. https://doi.org/10.1108/02644409510799532

Petley DN (2010) On the impact of climate change and population growth on the occurrence of fatal landslides in South, East and SE Asia. Q J Eng Geol Hydrogeol 43(4):487–496. https://doi.org/10.1144/1470-9236/09-001

Planet Team (2019) Planet Application Program Interface: In Space for Life on Earth. San Francisco, CA. https://api.planet.com. Accessed 20 Mar 2019

Preisig G, Eberhardt E, Smithyman M, Preh A, Bonzanigo L (2016) Hydromechanical rock mass fatigue in deep-seated landslides accompanying seasonal variations in pore pressures. Rock Mech Rock Eng 49(6):2333–2351. https://doi.org/10.1007/s00603-016-0912-5

Riegl LMS GmbH (2018) RiSCAN Pro version 2.6.

Riva F, Agliardi F, Amitrano D, Crosta GB (2018) Damage-based time-dependent modeling of paraglacial to postglacial progressive failure of large rock slopes. J Geophys Res Earth Surf 123(1):124–141. https://doi.org/10.1002/2017JF004423

Roberti G, Ward B, van Wyk de Vries B, Friele P, Perotti L, Clague JJ, Giardino M (2018) Precursory slope distress prior to the 2010 Mount Meager landslide, British Columbia. Landslides 15(4):637–647. https://doi.org/10.1007/s10346-017-0901-0

Rocscience (2016) DIPS 7. Rocscience Inc. Toronto Canada.

Semenza E, Ghirotti M (2000) History of the 1963 Vaiont slide: the importance of geological factors. Bull Eng Geol Environ 59(2):87–97. https://doi.org/10.1007/s100640000067

Shugar DH, Clague JJ (2011) The sedimentology and geomorphology of rock avalanche deposits on glaciers. Sedimentology 58(7):1762–1783. https://doi.org/10.1111/j.1365-3091.2011.01238.x

Sitar N, MacLaughlin MM, Doolin DM (2005) Influence of kinematics on landslide mobility and failure mode. J Geotech Geoenviron 131(6):716–728. https://doi.org/10.1061/(ASCE)1090-0241(2005)131:6(716)

Spreafico MC, Francioni M, Cervi F, Stead D, Bitelli G, Ghirotti M, Girelli VA, Lucente CC, Tini MA, Borgatti L (2016) Back analysis of the 2014 San Leo landslide using combined terrestrial laser scanning and 3D distinct element modelling. Rock Mech Rock Eng 49(6):2235–2251. https://doi.org/10.1007/s00603-015-0763-5

Spreafico MC, Franci F, Bitelli G, Borgatti L, Ghirotti M (2017a) Intact rock bridge breakage and rock mass fragmentation upon failure: quantification using remote sensing techniques. Photogramm Rec 32(160):513–536. https://doi.org/10.1111/phor.12225

Spreafico MC, Cervi F, Francioni M, Stead D, Borgatti L (2017b) An investigation into the development of toppling at the edge of fractured rock plateaux using a numerical modelling approach. Geomorphology 288:83–98. https://doi.org/10.1016/j.geomorph.2017.03.023

Stead D, Coggan J (2012) Numerical modeling of rock-slope instability. In: Clague JJ, Stead D (eds) Landslides: types, mechanisms and modeling. Cambridge University Press, Cambridge, pp 144–158

Stead D, Eberhardt E (2013) Understanding the mechanics of large landslides. In: Genevois R, Prestininzi A (eds). Proceedings of the International Conference on Vajont 1963-2013. Thoughts and analyses after 50 years since the catastrophic landslideItalian. Ital J Eng Geol Environ - Book Series 6:85–112. https://doi.org/10.4408/IJEGE.2013-06.B-07

Stead D, Wolter A (2015) A critical review of rock slope failure mechanisms: the importance of structural geology. J Struct Geol 74:1–23. https://doi.org/10.1016/j.jsg.2015.02.002

Sturzenegger M, Stead D (2012) The Palliser Rockslide, Canadian Rocky Mountains: characterization and modeling of a stepped failure surface. Geomorphology 138(1):145–161. https://doi.org/10.1016/j.geomorph.201

Vanneschi C, Di Camillo M, Aiello E, Bonciani F, Salvini R (2019) SfM-MVS photogrammetry for rockfall analysis and hazard assessment along the ancient Roman Via Flaminia Road at the Furlo Gorge (Italy). ISPRS Int J Geo Inf 8(8):325. https://doi.org/10.3390/ijgi8080325

Vivas JB (2014) Groundwater characterization and modelling in natural and open pit rock slopes. M.Sc. Thesis, Simon Fraser University

von Sacken R (1991) New data and re-evaluation of the 1965 Hope Slide, British Columbia. M.Sc. Thesis, University of British Columbia

Waddington BA (1995) The Fraser Glaciation in the Cascade Mountains, Southwestern British Columbia. M.Sc. Thesis, University of British Columbia.

Weichert D, Horner RB, Evans SG (1994) Seismic signatures of landslides: the 1990 Brenda mine collapse and the 1965 Hope rockslides. Bull Seismol Soc Am 84(5):1523–1532. https://doi.org/10.1785/0120070082

Westoby MJ, Brasington J, Glasser NF, Hambrey MJ, Reynolds JM (2012) "Structure-from-motion" photogrammetry: a low-cost, effective tool for geoscience applications. Geomorphology 179:300–314. https://doi.org/10.1016/j.geomorph.2012.08.021

Wetmiller RJ, Evans SG (1989) Analysis of the earthquakes associated with the 1965 Hope landslide and their effects on slope stability at the site. Can Geotech J 26(3):484–490. https://doi.org/10.1139/t89-062

Wolter A, Stead D, Clague JJ (2014) A morphologic characterisation of the 1963 Vajont Slide, Italy, using long-range terrestrial photogrammetry. Geomorphology 206:147–164. https://doi.org/10.1016/j.geomorph.2013.10.006

Wolter A, Gischig VS, Stead D, Clague JJ (2016) Investigation of geomorphic and seismic effects on the 1959 Madison Canyon, Montana, landslide using an integrated field, engineering geomorphology mapping, and numerical modelling approach. Rock Mech Rock Eng 49:2479–2501. https://doi.org/10.1007/s00603-015-0889-5

D. Donati (✉) · **D. Stead**
Department of Earth Sciences,
Simon Fraser University,
Burnaby, BC V5A 1S6, Canada
Email: davide_donati@sfu.ca

M.-A. Brideau
Westrek Geotechnical Services Ltd.,
Squamish, BC V8B 0K1, Canada

M. Ghirotti
Dipartimento di Fisica e Scienze della Terra,
University of Ferrara,
44122, Ferrara, Italy